

The C-Band All-Sky Survey (C-BASS): New Constraints on the Integrated Radio Spectrum of M 31

Stuart E. Harper,^{1*} Adam Barr,¹ C. Dickinson,^{1,2†} M. W. Peel,^{3,4,5} Roke Cepeda-Arroita,¹ C. J. Copley,⁶ R. D. P. Grumitt,⁷ J. Patrick Leahy,¹ J. L. Jonas,^{8,9} Michael E. Jones,⁷ J. Leech,⁷ T. J. Pearson,² A. C. S. Readhead,² Angela C. Taylor⁷

¹*Jodrell Bank Centre for Astrophysics, Department of Physics & Astronomy, The University of Manchester, Oxford Road, Manchester, M13 9PL, U.K.*

²*Cahill Centre for Astronomy and Astrophysics, California Institute of Technology, Pasadena, CA 91125, U.S.A.*

³*Instituto de Astrofísica de Canarias, E-38205 La Laguna, Tenerife, Spain*

⁴*Departamento de Astrofísica, Universidad de La Laguna (ULL), E-38206 La Laguna, Tenerife, Spain*

⁵*Imperial College London, Blackett Lab, Prince Consort Road, London SW7 2AZ, UK*

⁶*Ancera.com, 15 Commercial St, Branford, CT 06405, USA*

⁷*Sub-department of Astrophysics, University of Oxford, Denys Wilkinson Building, Keble Road, Oxford OX1 3RH, U.K.*

⁸*Department of Physics and Electronics, Rhodes University, Grahamstown, 6139, South Africa*

⁹*South African Radio Astronomy Observatory, 2 Fir Road, Observatory, Cape Town, 7925, South Africa*

Accepted XXX. Received YYY; in original form ZZZ

ABSTRACT

The Andromeda galaxy (M 31) is our closest neighbouring spiral galaxy, making it an ideal target for studying the physics of the interstellar medium in a galaxy very similar to our own. Using new observations of M 31 at 4.76 GHz by the C-Band All-Sky Survey (C-BASS), and all available radio data at 1° resolution, we produce the integrated spectrum and put new constraints on the synchrotron spectral index and anomalous microwave emission (AME) from M 31. We use aperture photometry and spectral modelling to fit for the integrated spectrum of M 31, and subtract a comprehensive model of nearby background radio sources. The AME in M 31 is detected at 3 σ significance with a peak near 30 GHz and flux density 0.27 ± 0.09 Jy. The synchrotron spectral index of M 31 is flatter than our own Galaxy at $\alpha = -0.66 \pm 0.03$ with no strong evidence of spectral curvature. The emissivity of AME, averaged over the total emission from M 31 is lower than typical AME sources in our Galaxy, implying that AME is not uniformly distributed throughout M 31 and instead is likely confined to sub-regions—this will need to be confirmed using future higher resolution observations around 20–30 GHz.

Key words: galaxies: individual: M31 – galaxies: ISM – radiation mechanism: non-thermal – radiation mechanism: thermal – diffuse radiation – radio continuum: ISM

1 INTRODUCTION

The Andromeda Galaxy, also known as Messier 31 (M 31), is the closest spiral galaxy to our Galaxy, its radio continuum extent subtending $\approx 2.7^\circ \times 1^\circ$ on the sky (Berkhuijsen et al. 1983). The proximity of M 31 and its similarities to our own Galaxy have made it an ideal target for testing our understanding of the interstellar medium (ISM) and it has been studied at many wavelengths from radio (e.g., Brown & Hazard 1950; Beck et al. 1980; Berkhuijsen et al. 2003), to IR/sub-mm (e.g., Gordon et al. 2006; Fritz et al. 2012; Planck Collaboration et al. 2015), optical (e.g., Lauer et al. 1993) and UV (e.g., Code & Welch 1979). Together these observations have greatly improved our understanding of a range of physical phenomena within M 31, from the synchrotron emission emitted by cosmic rays, to thermal dust

properties, and the physics of star-formation within a galaxy like our own.

At radio frequencies ($\lesssim 100$ GHz) the emission from normal galaxies is typically due to synchrotron and free-free processes, while at higher frequencies ($\gtrsim 100$ GHz) thermal dust radiation dominates. Anomalous microwave emission (AME), first observed several decades ago (Kogut et al. 1996; Leitch et al. 1997), is a fourth component that is characterized by a spectrum that is peaked around 30 GHz. The most favoured model for AME is that it is generated by rapidly rotating spinning dust grains (Draine & Lazarian 1998; Ali-Haïmoud et al. 2009). AME has been found in a range of Galactic structures from high Galactic latitude cirrus clouds (e.g. Davies et al. 2006; Planck Collaboration XII 2014; Harper et al. 2022), to individual dust clouds and HII regions (Watson et al. 2005; Casassus et al. 2008; Cepeda-Arroita et al. 2021; Rennie et al. 2022). Yet, AME in other galaxies seems to be far less prevalent with little or no evidence of AME in the integrated spectra of several spiral galaxies (Peel et al. 2011; Bianchi et al. 2022), and the only clear detection of

* E-mail: stuart.harper@manchester.ac.uk

† E-mail: clive.dickinson@manchester.ac.uk

AME in external galaxies being confined to individual star-forming regions (Hensley et al. 2015; Murphy et al. 2018). When estimating the average emissivity of the AME (i.e., the AME brightness per unit dust column) from other galaxies we find that it is much lower than known sources of AME implying that AME is generally not uniformly distributed throughout the ISM. A detailed review of current AME science can be found in Dickinson et al. (2018).

The first attempt to characterise AME in M 31 used a combination of WMAP and *Planck* data alongside older radio surveys (Planck Collaboration et al. 2015), and found there is a tentative evidence for AME in the integrated spectrum of M 31. Later, observations at ≈ 6 GHz by the Sardinian Radio Telescope (SRT) completely changed the prospect of AME in M 31, suggesting that AME is the dominant emission component at 30 GHz and the emissivity was similar to that observed in our own galaxy (Battistelli et al. 2019)—something not found in other galaxies, or by the Planck Collaboration et al. (2015) analysis.

We revisit the integrated spectrum of M 31 using observations from the C-Band All Sky Survey (C-BASS) at 4.76 GHz (Taylor et al. in prep.), and the publicly available QUI Joint Tenerife Experiment (QUIJOTE) wide survey (Rubiño-Martín et al. 2023) observations at 11 to 19 GHz. These two surveys fill in the gap between WMAP/*Planck* microwave frequencies and lower frequency radio data. Unlike the SRT data, the C-BASS and QUIJOTE observations have resolutions comparable to the other surveys, making them ideal for constraining the low frequency spectrum of M 31.

The paper is structured as follows: In Section 2 we give an overview of the C-BASS experiment and the ancillary datasets used. In Section 3 we give an overview of how we perform aperture photometry and the model fitted to the SED of M 31. Section 4 describes how we model and remove other extragalactic radio sources from the region around M 31. In Section 5 we present the main results, followed by a discussion in Section 6. Finally, Section 7 summarises the main conclusions.

2 DATA

2.1 C-BASS

The C-Band All Sky Survey (C-BASS) is a ground-based full-sky survey of total intensity and polarisation at a frequency of 4.76 GHz (Jones et al. 2018). The survey has an angular resolution of $0^{\circ}.73$ full-width half-maximum (FWHM). C-BASS observed the northern hemisphere from the Owens Valley Radio Observatory in California, USA, and observations of the southern sky are ongoing at Klerefontein, South Africa. In this work we use the C-BASS North total intensity data that has been deconvolved to a Gaussian beam with a FWHM of 1° . Below we give a brief summary of the C-BASS instrument, data processing, and maps; full details will be published in Taylor et al. (in prep.).

The C-BASS North telescope is a 6.1 m Gregorian antenna. To suppress sidelobe pick-up and symmetrise the beam response the primary antenna was under-illuminated; a radio-absorbing baffle surrounded the edge of the primary; and the struts supporting the secondary were replaced with a low-loss dielectric cone (Holler et al. 2013). The telescope beam contains 73 per cent of the power in the main beam, and 95 per cent within $9^{\circ}.2$ radius.

The receiver was a cryogenically cooled dual circularly polarised correlation receiver that allows for the simultaneous measurement of Stokes I, Q, and U. The receiver has a nominal bandwidth of 4.5–5.5 GHz, but the effective bandwidth was 0.5 GHz due to notch filters

installed around the centre of the band to suppress fixed terrestrial radio frequency interference (RFI) (King et al. 2014).

C-BASS North observations were taken between 2012 November and 2015 March, with a total observing time of approximately 2000 hours. The observing strategy was to perform 360° azimuth sweeps at fixed elevations. The total sky area covered was 26000 sq. degrees and the minimum declination observed was -15° .

The C-BASS north data processing pipeline will be described in detail in Taylor et al. (in prep.). The data processing includes masking transient RFI and solar system objects, modelling and subtracting ground emission, and suppressing a microphonic 1.2 Hz oscillation in the time-ordered data (TOD) that is due to the receiver cryogenics.

The C-BASS maps are made using the Descart (Sutton et al. 2010) implementation of the destriping map-making method. Destriping map-making fits offsets to the time correlated $1/f$ noise in the C-BASS TOD by using the covariance of the sky signal and C-BASS observing strategy. Jack-knife tests of the C-BASS data found that residual $1/f$ noise and other systematics after map-making are less than a 1 per cent on scales of the C-BASS beam.

The absolute temperature scale of the C-BASS map was set by the WMAP models of the flux density and secular changes of the supernova remnant Taurus A (Tau A) (Weiland et al. 2011). The flux density models for such bright calibrator sources (e.g., Cas A and Tau A) are known to ≈ 0.5 per cent precision, providing a precise absolute calibration scale. The band-averaged central frequency of C-BASS when calibrated against a flat-spectrum source ($\beta = -2$ in brightness temperature units) was 4.76 GHz. The calibration uncertainty of the C-BASS intensity map has additional contributions from colour corrections, and the beam model. The total calibration uncertainty of the C-BASS North map is conservatively assumed to be 3 per cent.

2.2 Ancillary Data

We use additional surveys at radio and infrared bands to fully sample the spectrum of M 31 around the peak in the spinning dust emission. A summary of these ancillary data is given in Table 1. All maps are smoothed to a common 1° resolution and repixelized into HEALPIX $N_{\text{side}} = 256$ maps.

The well-known Haslam 408 MHz map is used to constrain low-frequency emission (Haslam et al. 1981, 1982). We use the version of the 408 MHz map that was reprocessed by Remazeilles et al. (2015), which significantly reduces the striping artefacts due to $1/f$ noise along the scan directions. The survey has a native resolution of approximately 56 arcmin FWHM. The 408 MHz survey is calibrated against an absolutely calibrated 404 MHz survey (Pauliny-Toth & Shakeshaft 1962) with a nominal calibration uncertainty of 5 per cent. However, uncertainties in the beam of the 408 MHz are not well known and can translate into scale-dependent changes in the flux density across the map that could be up to tens of percent. There are also residual $1/f$ noise stripes that can contribute up to 3.8 Jy per beam. As such, to account for all these effects we conservatively assign a 10 per cent calibration uncertainty to the 408 MHz data, similar to other analyses (e.g., Planck Collaboration et al. 2014).

The full-sky map at 1.42 GHz (Reich & Reich 1986, 1988) combines data from the German Stockert 25-m and Argentinian Villa Elisa 30-m telescopes to produce a full-sky map with 36 arcmin resolution. We use a destriped version of the map, calibrated using absolute sky horn measurements. It is common to apply a main-beam to full-beam correction factor of 1.55 to bring the absolute calibration onto the main-beam scale, however Planck Collaboration et al. (2015) suggests a factor of 1.3 would be better as the source is par-

Table 1. The integrated flux densities of M 31 for the three cases considered: without subtracting the CMB, subtracting the SMICA CMB model, and lastly subtracting our model of background radio sources at each frequency as well as the SMICA CMB model. We include the flux densities from the *Planck* (Planck Collaboration et al. 2015) and SRT analysis (Battistelli et al. 2019) for comparison.

Survey	Frequency (GHz)	Cal. ⁴ (%)	No CMB	CMB	CMB & Source	Planck Collaboration et al. (2015) ² (Jy)	Battistelli et al. (2019) ³
			subtraction (Jy)	Subtracted (Jy)	Subtracted (Jy)		
Haslam	0.408	10.0	17.5±1.9	17.5±1.9	18±2	23±4	18.4±1.6
SRT HI-1	1.385	5.0	–	–	–	–	5.4±0.4
Reich	1.42	10.0	8.5±0.7	8.5±0.7	8.4±0.7	–	–
SRT HI-2	1.437	5.0	–	–	–	–	5.3±0.4
C-BASS	4.76	3.0	4.06±0.14	4.06±0.14	4.04±0.14	–	–
SRT C-1	6.313	5.0	–	–	–	–	1.21±0.08
SRT C-2	6.938	5.0	–	–	–	–	1.19±0.09
QUIJOTE	12.0	5.0	2.73±0.16	2.75±0.16	2.48±0.16	–	–
WMAP	22.8	3.0	2.27±0.11	2.12±0.08	1.84±0.07	2.09±0.10	2.00±0.17
<i>Planck</i>	28.4	1.0	2.28±0.11	1.95±0.05	1.71±0.06	2.05±0.11	1.86±0.15
WMAP	33.0	3.0	2.11±0.15	1.85±0.08	1.54±0.08	1.88±0.14	1.71±0.21
WMAP	40.7	3.0	2.00±0.20	1.48±0.10	1.22±0.10	1.73±0.18	1.31±0.16
<i>Planck</i>	44.1	1.0	2.07±0.24	1.53±0.11	1.24±0.11	1.31±0.21	1.45±0.25
WMAP	60.7	3.0	3.6±0.4	2.27±0.20	1.90±0.20	2.9±0.4	1.7±0.4
<i>Planck</i>	70.4	1.0	3.5±0.6	1.83±0.24	1.51±0.24	3.3±0.5	2.1±0.4
WMAP	93.5	3.0	5.1±0.9	2.9±0.4	2.6±0.4	4.3±0.8	3.5±1.0
<i>Planck</i>	100.0	1.0	8.2±1.0	5.3±0.4	5.0±0.4	7.3±1.2	5.8±0.5
<i>Planck</i>	143.0	1.0	20.4±1.6	14.2±0.7	14.0±0.7	18.2±1.5	15.7±1.4
<i>Planck</i>	217.0	1.0	80±3	68.2±1.5	67.9±1.5	76±8	69±6
<i>Planck</i>	353.0	1.3	325±7	318±6	318±6	298±13	318±24
<i>Planck</i>	545.0	6.0	1054±65	1054±65	1054±65	1020±100	1027±73
<i>Planck</i>	857.0	6.4	3120±210	3120±210	3120±210	3050±310	3020±190
COBE-DIRBE	1249.0	13.5	5890±810	5890±810	5890±810	5700±770	–
COBE-DIRBE	2141.0	10.6	7310±810	7310±810	7310±810	7300±1000	–
COBE-DIRBE	3000.0	11.6	3570±440	3570±440	3570±440	3600±500	–

¹ We combine both the 11 and 13 GHz data into a single channel, see Section 2.2 for details.

² The *Planck* analysis includes contributions from the CMB and background sources.

³ The SRT analysis subtracted the a CMB model and background radio sources.

⁴ Calibration uncertainties for each survey are discussed in Section 2.1 and Section 2.2.

tially resolved. We adopt the factor of 1.3 for this analysis, but the results do not depend significantly on which factor is chosen. As with the 408 MHz data there are large uncertainties in this map related to the scale-dependent changes in flux density due to the beam, residual noise stripes, and the inherent calibration uncertainty. Reich & Reich (1988) give an uncertainty on the full-beam to main-beam ratio of approximately 5 per cent when directly comparing the flux density conversion factors of the Stockert data to that of an older radio survey, however when doing a comparison of these two surveys at a common resolution they find a 16 per cent scatter in the measured pixel brightnesses. Noting that these uncertainties include contributions from two surveys, and that there is no simple way to determine precisely full-beam to main-beam ratio for a resolved source like M 31 in the Stockert data, we assign the 1.42 GHz survey a conservative 10 per cent calibration uncertainty.

The QUI Joint Tenerife Experiment (QUIJOTE) Multi-Frequency Instrument (MFI) is a four horn focal plane array that observes between 10 and 20 GHz at 1° resolution (Rubiño-Martín et al. 2023). The QUIJOTE MFI wide survey data covers the entire Northern sky including M 31. We use the 2023 data release available on the NASA LAMBDA website¹. For this analysis we combine the MFI 11 and 13 GHz channels together and then smooth the combined map to 1° resolution assuming a weighted average of the FWHM for both the 11 and 13 GHz channels of 55.61 and a frequency of 12 GHz.

The reason for combining the maps is the high correlation in the noise between the two channels, which is 90–95 per cent in intensity (Rubiño-Martín et al. 2023). The 17 and 19 GHz channels do not have sufficient sensitivity to detect M 31 and are therefore excluded. The calibration uncertainty for the QUIJOTE MFI data is 5 per cent.

We use maps from the *Planck* NPIPE joint LFI and HFI reprocessing (Planck Collaboration et al. 2020b) with eight frequency bands ranging from 28.4 GHz to 857 GHz. It should be noted that this is different from the Planck Collaboration et al. (2015) analysis, which uses the maps from the 2015 data release. We do not use the 100 GHz and 217 GHz maps, as these frequency bands contain contamination from CO molecular lines (e.g., Planck Collaboration et al. 2014). This has a significant effect on the estimate of the flux densities at these frequencies, which in turn affects the modelling of the thermal dust emission. We adopt calibration uncertainties for the LFI of 3 per cent (Planck Collaboration et al. 2014) and HFI of 5 per cent (Planck Collaboration et al. 2020a); these uncertainties account for colour corrections, residual beam asymmetries, and other low-level systematic errors.

WMAP has five frequency bands: 22.8 GHz, 33.0 GHz, 40.7 GHz, 60.7 GHz and 93.5 GHz. The maps, smoothed to 1°, are the final 9-year maps (Bennett et al. 2013) stored in the LAMBDA² archive. A 3 per cent overall calibration uncertainty was applied to take into account potential low-level systematics such as beam asymmetries,

¹ https://lambda.gsfc.nasa.gov/product/qui_jote/index.html

² <https://lambda.gsfc.nasa.gov>

which was used by other studies (Planck Collaboration et al. 2014). We believe this is reasonable since we are not limited by instrumental noise.

Infrared surveys let us measure the (modified) blackbody curve of thermal dust at temperatures above ≈ 15 K. The COBE-DIRBE survey (Hauser et al. 1998), at $240\ \mu\text{m}$ (1249 GHz) and $140\ \mu\text{m}$ (2141 GHz) are used to measure the peak of the thermal dust spectrum. The Zodi-Subtracted Mission Average (ZSMA) maps are used, regridded to the HEALPix format.

3 PHOTOMETRY AND MODELLING

3.1 Spectral models

The integrated emission from M 31 is modelled as a combination of up to five components: synchrotron, free-free, spinning dust, thermal dust emission, and the CMB. The full model is defined as

$$S_{\text{total}}(\nu) = S_{\text{synch}}(\nu, A_{\text{synch}}, \alpha) + S_{\text{ff}}(\nu, \text{EM}) + S_{\text{AME}}(\nu, A_{\text{AME}}, \nu_{\text{AME}}) + S_{\text{td}}(\nu, \tau_{250}, T_{\text{td}}, \beta) + S_{\text{CMB}}(\nu, \Delta T), \quad (1)$$

where each contribution is explained in detail below.

The synchrotron emission is modelled as a simple power-law, with two free parameters:

$$S_{\text{synch}}(\nu) = A_{\text{synch}} \nu^\alpha, \quad (2)$$

where A_{synch} is the synchrotron amplitude at 1 GHz, ν is the frequency in GHz and α is the flux density spectral index. We also include an alternative synchrotron model that allows for spectral curvature:

$$S_{\text{synch}}(\nu) = A_{\text{synch}} \nu^{\alpha + C \log(\nu)}, \quad (3)$$

where C is the spectral curvature parameter.

The free-free flux density is converted from a free-free brightness temperature, T_{ff} , by

$$S_{\text{ff}} = \frac{2kT_{\text{ff}}\Omega\nu^2}{c^2}, \quad (4)$$

where k is the Boltzmann constant, Ω the solid angle of the aperture, and ν is the observing frequency. The free-free brightness temperature is given by

$$T_{\text{ff}} = T_e (1 - e^{-\tau_{\text{ff}}}), \quad (5)$$

where T_e is the electron temperature and τ_{ff} is the free-free optical depth. The optical depth τ_{ff} is given by Draine (2011)

$$\tau_{\text{ff}} = 5.468 \times 10^{-2} T_e^{-1.5} \nu_{\text{GHz}}^{-2} \text{EM} g_{\text{ff}}, \quad (6)$$

where EM (pc cm^{-6}) is the emission measure and g_{ff} is the Gaunt factor. We use the approximation for the Gaunt factor derived by Draine (2011):

$$g_{\text{ff}} \approx \ln \left\{ \exp \left[5.960 - \frac{\sqrt{3}}{\pi} \ln \left(Z_i \nu_{\text{GHz}} T_4^{-3/2} \right) \right] + e \right\}, \quad (7)$$

where e is Euler's constant, ν_{GHz} is the frequency in GHz, T_4 is the temperature in units of 10^4 K and Z_i is the charge on the scattering ions (assumed to be singly ionised). We use a fixed electron temperature of 8000 K, which is typical for most Galactic sources (Paladini et al. 2003), and only fit for EM. Such assumptions have negligible impact on the spectral model.

The thermal dust is modelled as a modified blackbody. It is fitted using

$$S_{\text{td}} = 2h \frac{\nu^3}{c^2} \frac{1}{e^{h\nu/kT_d} - 1} \tau_{250} (\nu/1.2\text{THz})^{\beta_d} \Omega, \quad (8)$$

where τ_{250} is the optical depth at $250\ \mu\text{m}$, T_d is the dust temperature, and β_d is the dust emissivity spectral index. Using a single-component modified blackbody model is a simplification of the thermal dust emission spectrum since we know in M 31 there will be many dust components with different emissivities, and temperatures. However, this approximation will only cause issues around the peak of the thermal dust emission spectrum at $\nu > 1000$ GHz, which is not critical for characterising the AME and the spectrum at lower frequencies.

We model the spinning dust component as a fixed template, produced using the SPDUST code (Ali-Haïmoud et al. 2009). The chosen template represents the warm neutral medium (WNM) as defined by Draine & Lazarian (1998), which is generally representative of AME regions (Dickinson et al. 2018). This template has a peak frequency of 28.1 GHz. The overall shape of the spinning dust spectrum is not strongly dependent on the environment in this analysis as the choice of environment mostly affects the spinning dust peak frequency and amplitude both of which are free parameters in this analysis. To fit the spinning dust component to an arbitrary peak frequency we interpolate the WNM model from SPDUST such that

$$S_{\text{AME}} = A_{\text{AME}} \frac{j(\nu \times \nu_{\text{WNM}}/\nu_0)}{j(\nu_r \times \nu_{\text{WNM}}/\nu_0)} \Omega, \quad (9)$$

where ν is the input frequency, ν_{WNM} is the peak frequency of the template (i.e. 28.1 GHz in flux density), ν_r is the reference frequency to fit the flux density to, and ν_0 is the fitted peak frequency. In this case we fit the flux density of the spinning dust curve at 28.4 GHz. We also tried other models such as the log-normal approximation (Stevenson 2014) or multi-component SPDUST models (Planck Collaboration et al. 2014) but these models require more free parameters that are not favoured by the data.

We model the contribution of the cosmic microwave background (CMB) anisotropies using

$$S_{\text{cmb}} = \frac{2k\nu^2}{c^2} \Omega \Delta T, \quad (10)$$

where ΔT is the mean CMB brightness over the aperture in thermodynamic units³, and the other symbols have their standard definitions.

3.2 MCMC Fitting

We use the EMCEE (Foreman-Mackey et al. 2019) implementation of the Markov Chain Monte Carlo (MCMC) to sample from our spectral model. Using an MCMC sampler to perform the model fitting is preferable to a more traditional least-squares method as it allows for a more complete interpretation of parameter correlations, and allows for the implementation of priors. We use 200 chains, each with 10000 samples, with a burn-in of 4000 samples for each spectral fit; these MCMC parameters were chosen as a balance between having a chain length that was sufficient for most chains to pass Gelman-Rubin convergence tests (Gelman & Rubin 1992) without using excessive computational resources. Any chains that had not converged after 10000 samples were reinitialised with starting parameters sampled

³ To convert Rayleigh-Jeans units (T_{RJ}) to thermodynamic units (T_{K}) we $T_{\text{RJ}} = T_{\text{K}} x^2 e^x / (e^x - 1)^2$ where $x = h\nu/kT_{\text{cmb}}$.

from the posterior distribution of the converged chains and then rerun for 10000 samples. Finally, we tested for sample-sample autocorrelation and found that a thinning the chains by 15 samples was sufficient to remove sample-sample correlations.

Starting parameters for the MCMC chains are calculated using the `PYTHON NUMPY Levenberg-Marquardt` least-squares implementation. We enforced positivity for all amplitude parameters (except for the CMB anisotropy amplitude). The impact of this prior is seen most in the determination of the emission measure (EM), which has a cut-off in its lower tail causing a slight underestimate of its uncertainty. The effect of the hard prior on EM can be seen in Figure 6.

We used the `FASTCC` package⁴ (Peel et al. 2022) to calculate colour corrections at the reference frequency given in Table 1 for each survey. The `FASTCC` code offers precalculated fits for a range of source spectral indices, utilising the measured bandpasses of several surveys, including: WMAP, *Planck*, QUIJOTE, and C-BASS. We integrated the `FASTCC` code into our spectral fitting, updating the colour corrections for each survey for the trial spectrum derived by each sample in the MCMC chains. Colour corrections typically alter the observed flux densities 1–2 per cent.

3.3 The CMB

At microwave frequencies the brightness of M 31 is comparable to the brightness of the CMB anisotropies at scales of a approximately 1° . In fact, between 70–100 GHz approximately half of the total flux density within the aperture is related to a CMB fluctuation. Therefore even small errors in the contribution of the CMB fluctuations could result in a relatively large error in the flux density at microwave frequencies. As such, the CMB contribution to M 31 must be carefully considered.

There are two ways to approach the CMB contribution: model the CMB anisotropies as an additional component in the spectral fitting, as was done in the *Planck* analysis (Planck Collaboration et al. 2015); or the CMB contribution can be subtracted from the maps using one of the *Planck* CMB solutions. The first solution is problematic since it is adding an additional parameter to the overall fit, and the CMB contribution is also highly degenerate with the other components (synchrotron, AME, and free-free emission) at microwave frequencies. The second solution of subtracting the CMB directly from the maps faces the question of the reliability of the various CMB solutions. When we include the CMB (best-fit parameters given in Table 2) we find we cannot easily constrain the CMB brightness within the aperture. We find the CMB brightness to be $0.3 \pm 1.1 \mu\text{K}$ in thermodynamic units, which is equivalent to $0.03 \pm 0.12 \text{ Jy}$ at 30 GHz and $0.2 \pm 1.0 \text{ Jy}$ at 100 GHz. We are not able to constrain the CMB anisotropies directly from the integrated spectrum, and even the uncertainties from the differences in the four CMB models, discussed in Section 3.5, are larger than the fitted CMB brightness. Measuring the flux density of the CMB anisotropies within the M 31 aperture using the CMB models gives a flux density of 0.2–0.3 Jy at 30 GHz—an order of magnitude larger than the fit predicts. Further, the CMB amplitude is highly degenerate with the free-free and AME amplitudes, and it appears the flux density of the CMB anisotropies are being absorbed into the free-free emission measure parameter. It is for these reasons that we do not favour fitting for the CMB spectrally, but opt instead to subtract it using one of the available CMB models.

In Figure 1 we show a side-by-side comparison of the *Planck* 217 GHz map with the four *Planck* CMB solutions: Independent

Component Analysis of power spectra (SMICA; Cardoso et al. 2008); needlet-based internal linear combination (NILC; Delabrouille et al. 2009); Commander—a pixel-based parameter fitting method (Eriksen et al. 2008); and a multi-resolution internal template cleaning method (SEVEM; Fernández-Cobos et al. 2012). There is a CMB fluctuation around the lower-right edge of the disk that is as bright as, and at many frequencies brighter than, the emission from M 31 itself. It has been suggested it may not be a CMB fluctuation but may be associated with cold gas clouds in the M 31 halo (De Paolis et al. 2014; Tahir et al. 2022) though we did not consider this possibility for this analysis. The four different CMB solutions are very similar, although there are low-level residuals of the molecular disk of M 31 in the SEVEM and NILC solutions. The SMICA and Commander solutions are very similar, with a negligible M 31 residual.

Comparing the aperture photometry of M 31 when using each of the four different CMB maps shows that at 22.8 GHz the largest change in flux density between all of the models is $\Delta S = 0.1 \text{ Jy}$, which is approximately 5 per cent of the total flux density measured. At 70.4 GHz, where the CMB is the dominant component, the largest difference is $\Delta S = 0.8 \text{ Jy}$ between the CMB components—approximately 50 per cent of the total measured flux density. We find that the Commander solution has the highest flux density, while the SMICA solution gives the lowest flux density. We therefore choose to use the SMICA solution to subtract the CMB from the WMAP and *Planck* data.

3.4 Aperture Photometry

Table 1 presents the flux density and uncertainty, excluding colour corrections, at each frequency. We do not include colour corrections to enable direct comparison between our analysis and the *Planck* (Planck Collaboration et al. 2015) and SRT (Battistelli et al. 2019) analyses. The *Planck* flux densities have not had the CMB or background sources subtracted, while the SRT flux densities have had both the CMB and background sources subtracted.

We used aperture photometry to construct an integrated flux density spectrum of M 31 using apertures matched to those used in the *Planck* analysis (Planck Collaboration et al. 2015) and the more recent analysis by the SRT (Battistelli et al. 2019). We used an elliptical aperture encompassing the entirety of M 31. The semi-major axis of the aperture is 100 arcmin, with a minor-to-major ratio is 0.7, and a position angle of 45° relative to Galactic North⁵.

To estimate the background emission, we determined the median of the pixels within an elliptical annulus with an inner and outer semi-major axis of 110 arcmin and 154 arcmin respectively. This annulus is 4 arcmin wider than that used by the *Planck* and SRT analyses. We left a 10 arcmin gap between the aperture and annulus to minimize the over-subtraction of source flux density that was smoothed outside of the aperture. Figure 2 shows the aperture and annulus used for three bands: C-BASS, WMAP *K-band* (22.8 GHz), and *Planck* 857 GHz.

3.5 Photometry Uncertainties

The uncertainty, σ_S^2 , in the measured flux density, S , has several contributions: the pixel noise uncertainty within the aperture, the uncertainty in the mean of the background annulus, the calibration uncertainty of the survey (given in Table 1), the uncertainty in the background radio source brightnesses, and the background emission

⁴ www.github.com/mpeel/fastcc

⁵ The solid angle of the aperture was $\Omega = 3.72 \times 10^{-3} \text{ sr}$

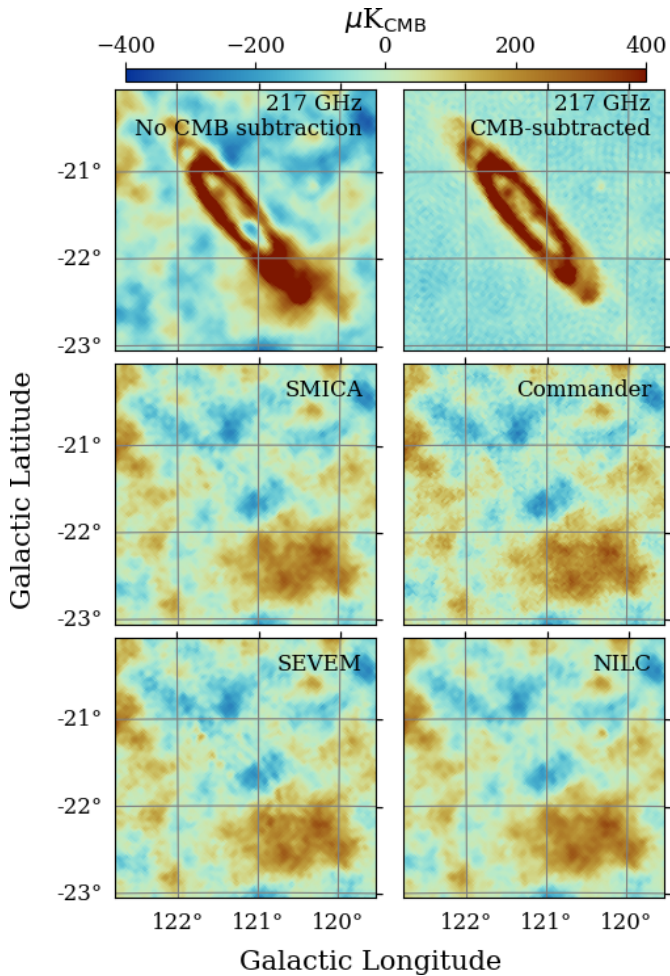


Figure 1. *Top row:* Planck 217 GHz data before and after subtraction of the SMICA CMB solution. *Middle row:* SMICA and Commander CMB solutions. *Bottom row:* SEVEM and NILC CMB solutions. These maps are shown at 5 arcmin resolution to show the M31 residuals in the CMB maps, however the fluctuations will be substantially smaller when smoothed to the 1° resolution used in the analysis.

uncertainty. We define the uncertainty in the flux density at each frequency as

$$\sigma_S^2 = \sigma_{\text{annu}}^2 N_S \left[1 + \frac{\pi}{2} \frac{N_S}{N_{\text{annu}}} \right] + S^2 \delta_g^2 + \sigma_{\text{src}}^2 + \sigma_{\text{cmb}}^2 N_S, \quad (11)$$

where N_S and N_{annu} are the number of pixels in the aperture and annulus respectively, σ_{annu} is the standard deviation of the annulus, δ_g is the calibration uncertainty, σ_{src} is the uncertainty from the background radio sources, and σ_{cmb} is the uncertainty due to residuals after subtracting a model of the CMB.

To estimate σ_{src}^2 we used the model uncertainties associated with each source fit (as described in Section 4.1). We calculate the model variance for each source at each frequency and sum over all of these to create a source variance map. The source aperture variance (σ_{src}^2) is simply the quadrature sum of the source variances within the aperture.

There is no simple way to determine the correlated systematics errors associated with the four CMB solutions in the region around M31 (i.e., it is possible all four maps are subtracting some flux density associated with M31). However, we can use the differences

between all four CMB solutions to obtain a lower limit on the CMB uncertainty, which we refer to as σ_{cmb} in Equation 11. To do this we created the six possible unique difference maps between the SMICA, NILC, SEVEM, and Commander CMB solutions. We then considered two methods to estimate the uncertainty in the CMB solutions. First, we measured the integrated flux density of each difference map, and took the standard deviation between them. At 30 GHz the typical uncertainty from the CMB was 0.041 Jy, while at 70 GHz it was 0.20 Jy. In thermodynamic units the uncertainty in the CMB was 1.34 μK . The second method was to measure the mean standard deviation of the pixels within the aperture for each difference pair. In this case we found the uncertainty in the CMB, near M31, was 1.55 μK . For σ_{cmb} , we used the average of these two uncertainties to get $\sigma_{\text{cmb}} = 1.45 \mu\text{K}$, which is scaled to each frequency. As stated earlier, this will be an underestimate of the total CMB uncertainty as this method cannot account for correlated errors between all four CMB solutions.

In Table 1, we show the measured flux densities with and without subtracting a CMB model. After subtracting the CMB, we find that the uncertainty in the flux density decreases. This is because the CMB fluctuations contributing to the uncertainty from within the annulus are greater than the additional uncertainty resulting from the differences in the CMB models. For instance, we note that in the frequency range of 70–100 GHz, when the CMB is not subtracted, the uncertainties are approximately 3 times larger than when the CMB is subtracted. This is because the CMB at these frequencies is the dominant source of emission. For example, at 30 GHz the typical RMS due to the CMB anisotropies within the annulus is 0.11 Jy, while the uncertainty due to CMB model subtraction is just 0.041 Jy.

4 EXTRAGALACTIC POINT SOURCES

4.1 Source Fitting and Subtraction

The spectral energy density (SED) of each source was modelled using a simple power-law, or a curved power-law model. Fits were performed on all available radio data between 0.1 and 100 GHz. More details about each source and the source catalogue are given in Appendix A. For sources modelled by a simple power-law relationship we used

$$f(\nu) = A \left(\frac{\nu}{\nu_r} \right)^\alpha, \quad (12)$$

where A is the amplitude, ν_r is a fixed reference frequency at 1 GHz, and α is the source spectral index. For sources with curved spectra we included a curvature term into the power-law fit, changing Equation 12 to

$$f(\nu) = A \left(\frac{\nu}{\nu_r} \right)^{\alpha + C \log(\nu)}, \quad (13)$$

where C is the curvature term. The models were fit using the SciPy⁶ implementation of the L-BFGS-B algorithm (Byrd et al. 1995) in the MINIMIZE package.

We used the Akaike information criterion (AIC, Akaike 1974) to determine which model was preferred for each source. As we have a small number of measurements per source, we use the corrected AIC statistic that modifies the penalty function for small sample sizes

⁶ <https://scipy.org/>

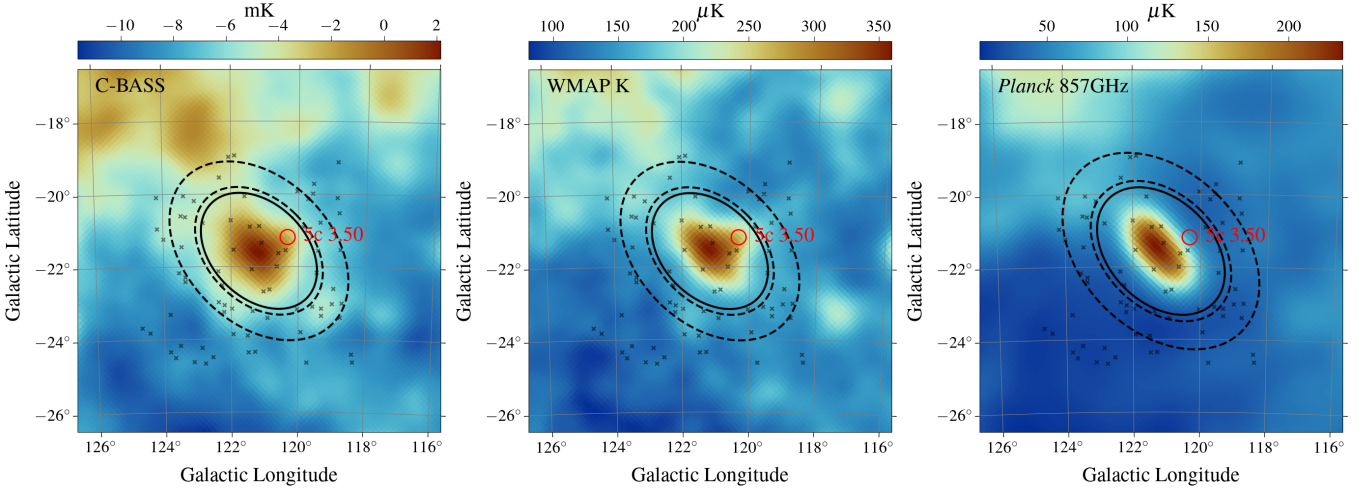


Figure 2. M 31 as seen at 4.76 GHz by C-BASS (left), WMAP *K*-band (22.8 GHz, middle), and Planck 857 GHz (right), after smoothing to 1° . The flux density was measured from pixels within the inner ellipse, while the background was estimated from the pixels between the inner and outer ellipses. The gray markers indicate the location of known radio sources. The brightest source at 4.76 and 22.8 GHz is 5C 3.50, which we mark with a red circle. All maps have had the SMICA CMB solution subtracted.

(AICc). The AICc is defined as

$$\text{AICc} = -2\mathcal{L} + \frac{2k^2 + 2k}{n - k - 1}, \quad (14)$$

where \mathcal{L} is the maximum of the log-likelihood, k is the number of model parameters, and n is the number of measurements. We find that for the majority of sources a simple power law is sufficient, with several sources modelled using a curved power-law (see Table A1). We used the model with the lowest AIC value as the best-fitting model for each source.

For many sources in the source catalogue (Appendix A) the uncertainty in the catalogue was either very small (less than 1 per cent) or was not given at all. In these instances we set the uncertainty to be 10 per cent of the flux density.

4.2 5C3.50

The brightest extragalactic background source at frequencies 5–70 GHz is the AGN 5C 3.50 (referred to as B3 0035+413 in Battistelli et al. 2019). In Figure 3 we show the spectrum of 5C 3.50 from radio to infrared frequencies. We can see that at frequencies less than 100 GHz the source has a flat spectrum and is steeply falling at higher frequencies. The peak flux density of the source is ≈ 0.6 Jy at 5 GHz, which is about 15 per cent of the total flux density within the aperture at 5 GHz, and similarly it accounts for 24 per cent of the total flux density at 30 GHz. Therefore it is critical to determine an accurate model of the source flux density.

Complicating the model of 5C 3.50 are indications of variability, which is to be expected from a compact AGN. Evidence of the variability of 5C 3.50 can be seen in the inset spectrum of Figure 3, where we can see between 4 and 8 GHz there is a jump in flux density by a factor of two. We also see evidence for variability within frequency bands, for example the flux density for 5C 3.50 at 1.4 GHz measured by the Very Large Array (VLA, Condon et al. 1998) was 0.692 ± 0.021 Jy in 1998, while the flux density reported by the Green Bank Telescope (GBT, White & Becker 1992) was 0.404 Jy (no uncertainty was reported) in 1992; a 50 per cent change in a 6 year period.

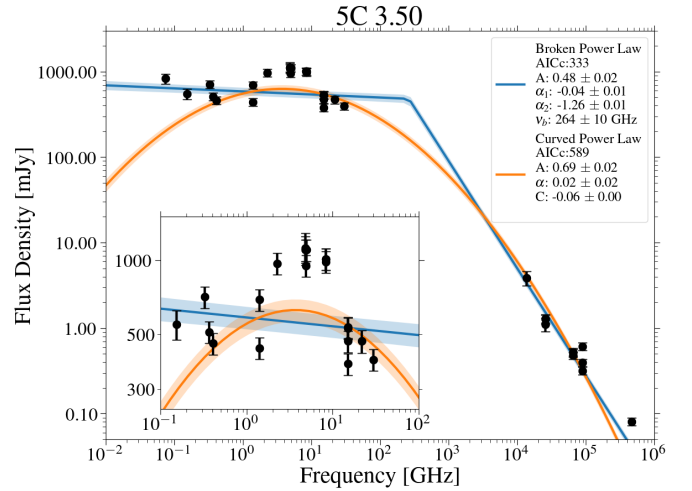


Figure 3. Ancillary data on 5C 3.50 (B3 0035+413), the brightest extragalactic background source near M 31. Fits for the broken power-law (blue) and curved power-law (orange) models are shown with the shaded areas indicating the 1σ model uncertainties. The inset shows a zoom-in of the radio data between 0.1–100 GHz. The legend shows the AICc and best-fit parameters for the curved power-law (Equation 13) and broken power-law (Equation 15) models.

To assess the variability of 5C 3.50, we used historical data covering 2009–2019 from the OVRO 40-m monitoring program (Richards et al. 2011). The data shows a steady decline in brightness from 0.59 ± 0.01 Jy in 2009 to a minimum of 0.32 ± 0.01 Jy in 2019. This decline covers the period when most observations used in this analysis were in progress, but does not include the period when WMAP data were being taken (2001–2010). To observe the effect this source has on the data, we looked at the single-year data from WMAP and found that, on average, most years are within 1σ of the survey average flux density, but there were significant drops in flux density in 2002 and 2006. The change in flux density in 2002 and 2006 were $\Delta S_{2002} = -0.26 \pm 0.11$ Jy and $\Delta S_{2006} = 0.30 \pm 0.11$ Jy, re-

spectively. If these drops in the flux density of M 31 were associated with 5C 3.50 then that would imply a change in the flux density of 5C 3.50 of 40 per cent relative the model average given in Table A1. The yearly data from the *Planck* 28.4 GHz data (2009 to 2012) also shows that there is significant evidence for variations in the brightness of 5C 3.50, its flux density changing slowly between 2009 and 2012 by 30–50 per cent—similar to the largest changes seen within the WMAP data. Figure 4 shows the measured flux densities from WMAP and *Planck* for each year. Overall, the impact of the variability of 5C 3.50 over the most critical frequency range of 10–100 GHz is significant but does not exceed 10 per cent of the total flux density of M 31. At 30 GHz this would constitute a maximum flux density change of approximately 0.2 Jy.

For 5C 3.50 we fit the SED over all available radio and infrared data. We do not fit over the narrower range of frequencies because of the broad peak at 4–8 GHz that is shown in the inset panel of Figure 3, which may be from source variability over the ten year time span of all the radio observations. It is also possible that the peak is a real structure in the spectrum of 5C 3.50 due to processes such as synchrotron self-absorption, but further observations would be needed to confirm this. We fit the SED of 5C 3.50 for both the curved power-law model (Equation 13) and an additional broken power-law model defined as:

$$f(\nu) = A \left(\frac{\nu}{\nu_b} \right)^{\alpha(\nu)}, \quad (15)$$

where $\alpha(\nu)$ at frequencies less than the break frequency, ν_b , are α_1 and α_2 at frequencies greater than ν_b . The functional form of $\alpha(\nu)$ was

$$\alpha(\nu) = \alpha_1 + S(\nu - \nu_b) (\alpha_1 - \alpha_2), \quad (16)$$

where S is a sigmoid function defined as $S(x) = (1 + e^{-x})^{-1}$. Using this model we find that at radio frequencies below the best-fit break frequency ($\nu_b = 264 \pm 14$ GHz) the spectrum can be described by a power-law with a spectral index of $\alpha_1 = -0.036 \pm 0.010$, and at higher frequencies the source has a steeper spectral index of $\alpha_2 = -1.25 \pm 0.010$. To account for the variability of 5C 3.50 we add an additional 10 per cent uncertainty at each frequency, which is the dominant source of uncertainty shown in the models in Figure 3.

5 RESULTS

We present the best-fitting spectral energy distribution (SED) after subtracting the SMICA CMB solution and background radio sources in Figure 5. The best-fitting parameters are listed in Table 2, alongside those given in Battistelli et al. (2019) and Planck Collaboration et al. (2015). Our preferred model is the "AME & power-law synchrotron" model in Table 2. For this section and Section 6, unless explicitly stated, all comparisons between models will be between our preferred model and the other models listed in Table 2.

In Figure 5 we can clearly see that at all frequencies spinning dust emission is sub-dominant to the synchrotron component. We find that when fitting for spinning dust emission we find a 3σ detection of $A_{\text{AME},30} = 0.27 \pm 0.09$ Jy, which is a similar to significance to that of the *Planck* analysis (Planck Collaboration et al. 2015) but is much less significant than the SRT measurements (Battistelli et al. 2019). The biggest difference between this analysis and the SRT analysis is the constraint of the lower frequency synchrotron emission. We can see that the SRT measurements at 6.313 GHz are four times fainter than the C-BASS measurements at 4.76 GHz in Table 1. The substantially steeper estimate of the M 31 synchrotron spectrum from the SRT

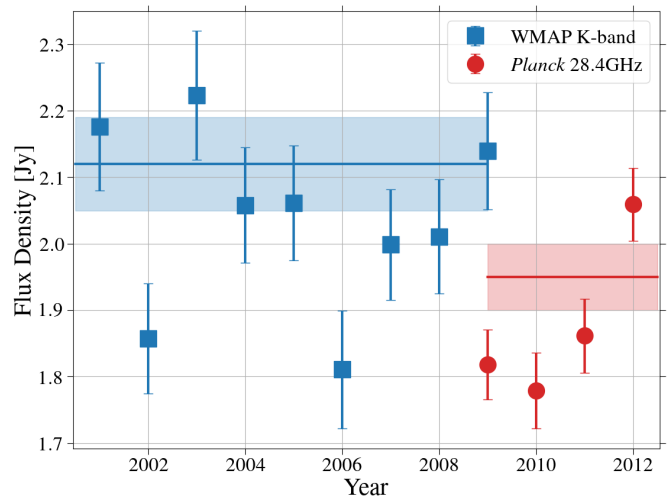


Figure 4. Integrated flux density of M 31 (including 5C 3.50) from WMAP 22.8 GHz and *Planck* 28.4 GHz data for each year between 2001 and 2012. We use the same aperture photometry parameters as with the main analysis (described in Section 3) but do not subtract nearby sources. The variations in the flux density is a combination of measurement error and true variations in the flux density of 5C 3.50. The solid lines and highlighted regions show the measured flux densities at 22.8 and 28.4 GHz from Table 1.

models therefore predicts a far larger spinning dust component to make up for the lower synchrotron emission at 30 GHz. However, with C-BASS the predicted synchrotron spectrum is closer to that of previous studies, and the spinning dust is similarly small. We believe that the main reason for the differences between the SRT and C-BASS measurements is due to spatial filtering in the SRT data, this is discussed more in Section 6.

In Figure 6 we show the posterior distributions of each parameter for the model with the CMB and sources subtracted, AME included, and a power-law synchrotron model. The figure shows that for most parameters the posterior is peaked. The emission measure (EM) parameter however shows a sharp cut-off due a hard positivity prior we enforce. As such, the EM uncertainties are underestimated in Table 2 for all model configurations, but it is especially underestimated for the model shown in Figure 5 as we do not make a significant detection.

Figure 6 also shows that there is a correlation between the EM, the synchrotron parameters (A_{sync} and α) and the spinning dust amplitude ($A_{\text{AME},30}$). This is expected, and was also seen in Planck Collaboration et al. (2015), because a lower amplitude, steeper spectrum synchrotron component would require additional contributions from either the EM or spinning dust components to explain the flux density observed around 20–70 GHz. The strong correlation between the thermal dust parameters in Figure 6 is the well-known dust temperature– β correlation caused by combination of effects such as noise uncertainties, multiple dust grain environments, and the physics of the dust grain emission (e.g., Shetty et al. 2009; Ysard et al. 2012).

It is possible to model AME using a log-normal distribution as has been shown in several analyses (Stevenson 2014; Cepeda-Arroita et al. 2021). However, fitting a log-normal distribution requires the introduction of an additional width parameter. We found that when using this model the width parameter was highly degenerate with the EM parameter, implying that the data do not support this additional parameter.

We find that the spectral index of the synchrotron emission is

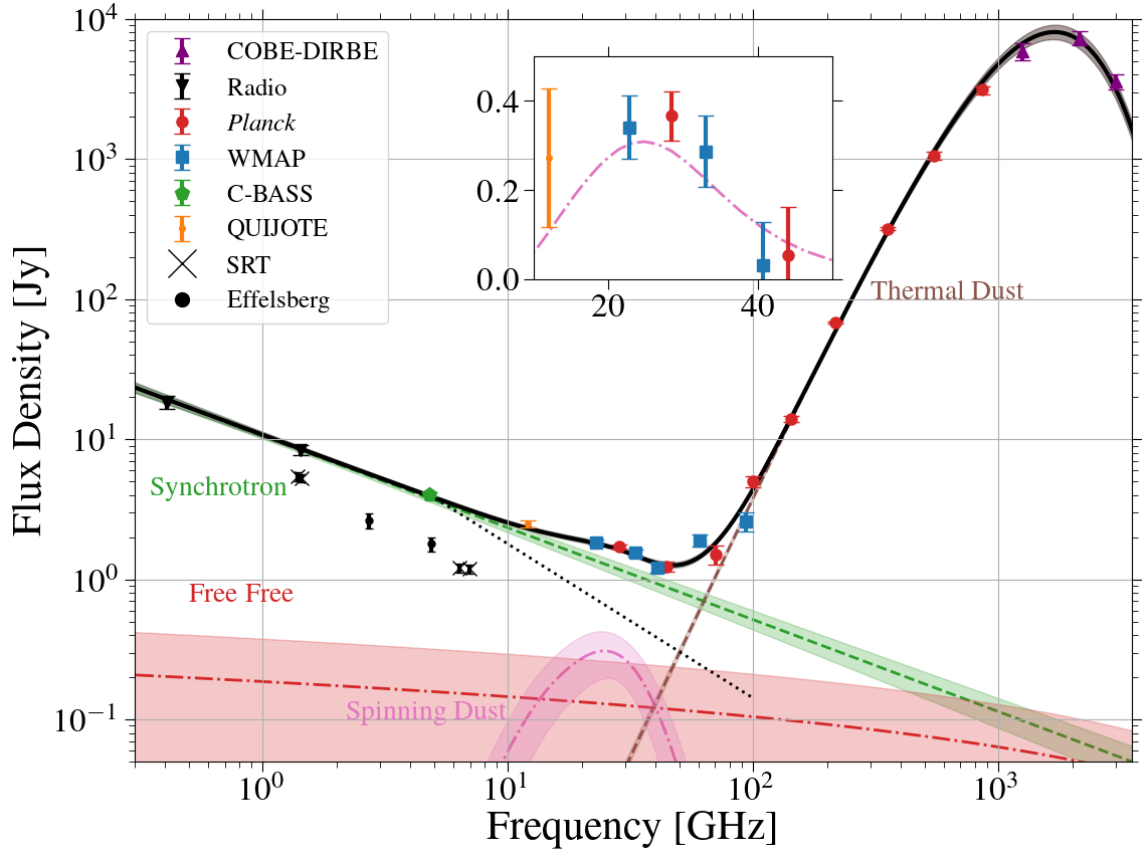


Figure 5. Integrated flux density spectrum for the M 31 after subtracting the SMICA CMB solution and background radio sources. Four emission components are fitted for: synchrotron, free-free, thermal dust, and spinning dust emission. The inset spectrum shows the residual flux density after subtracting all but the spinning dust model in the region around the fitted spinning dust peak frequency. We include the flux densities measurements from the SRT (Battistelli et al. 2019) and the Effelsberg (Beck et al. 2020) observations of M 31 for reference but these were not used in the fit. The black-dotted line shows the best-fit synchrotron spectral index from Battistelli et al. (2019) with the amplitude referenced to the C-BASS flux density measurement at 4.76 GHz.

Table 2. Mean posterior parameter estimates for the four cases discussed in the text. For comparison we include the previous parameter fits from the *Planck* and SRT analyses.

Parameter	No CMB Subtraction	CMB Subtracted	CMB & Source Subtracted			<i>Planck</i> 2015	SRT 2019
			AME & Power-Law ¹ Synchrotron	AME & Curved Synchrotron	No AME & Power-Law Synchrotron		
A_{sync} (Jy)	8.3 ± 0.8	9.7 ± 0.6	10.6 ± 0.5	10.2 ± 0.6	9.9 ± 0.5	9.5 ± 1.1	7.0 ± 0.5
α	-0.73 ± 0.10	-0.63 ± 0.05	-0.66 ± 0.03	-0.60 ± 0.06	-0.61 ± 0.04	-0.92 ± 0.16	-1.10 ± 0.09
C	–	–	–	-0.04 ± 0.03	–	–	–
EM (cm^{-6} pc)	3.9 ± 1.5	1.1 ± 0.8	0.4 ± 0.4	1.1 ± 0.8	0.9 ± 0.6	1.8 ± 1.3	1.1 ± 0.9
δ_T (μK)	0.3 ± 1.1	–	–	–	–	–	–
T_d (K)	19.5 ± 0.8	17.3 ± 0.4	17.2 ± 0.4	17.3 ± 0.4	16.9 ± 0.4	18.2 ± 1.0	18.8 ± 0.5
τ	1.06 ± 0.19	1.78 ± 0.18	1.84 ± 0.19	1.79 ± 0.19	2.00 ± 0.2	1.2 ± 0.2	–
β	1.44 ± 0.09	1.76 ± 0.05	1.77 ± 0.05	1.76 ± 0.05	1.81 ± 0.04	1.62 ± 0.11	1.49 ± 0.06
$A_{\text{AME},30}$ (Jy)	0.18 ± 0.15	0.32 ± 0.11	0.27 ± 0.09	0.38 ± 0.12	–	0.7 ± 0.3	1.45 ± 0.18
ν_{AME} (GHz)	35 ± 13	25 ± 2	24 ± 2	26 ± 2	–	–	–
χ^2	9.8	20.6	18.7	18.6	26.5	–	–
χ_r^2	1.4	2.6	2.3	2.3	2.9	–	–
AIC	107	110	106	106	119	–	–

¹ This is the preferred model that we refer to most often in the main text.

flatter ($\alpha = -0.66 \pm 0.03$) than the spectral indices in Battistelli et al. (2019) or Planck Collaboration et al. (2015), and is more typical of other galaxies (Condon et al. 1998). This is much flatter than the synchrotron spectrum found in our Galaxy, which typically has a spectral index of $\alpha = -1$ at frequencies of $\nu > 5$ GHz (e.g., Harper

et al. 2022). However, nearer the Galactic plane there is evidence that synchrotron emission is flatter (e.g. Kogut et al. 2007; Fuskeland et al. 2014), which will be the dominant component when measuring the integrated emission from a galaxy.

In Table 2 we compare the χ^2 residuals and the Akaike Information

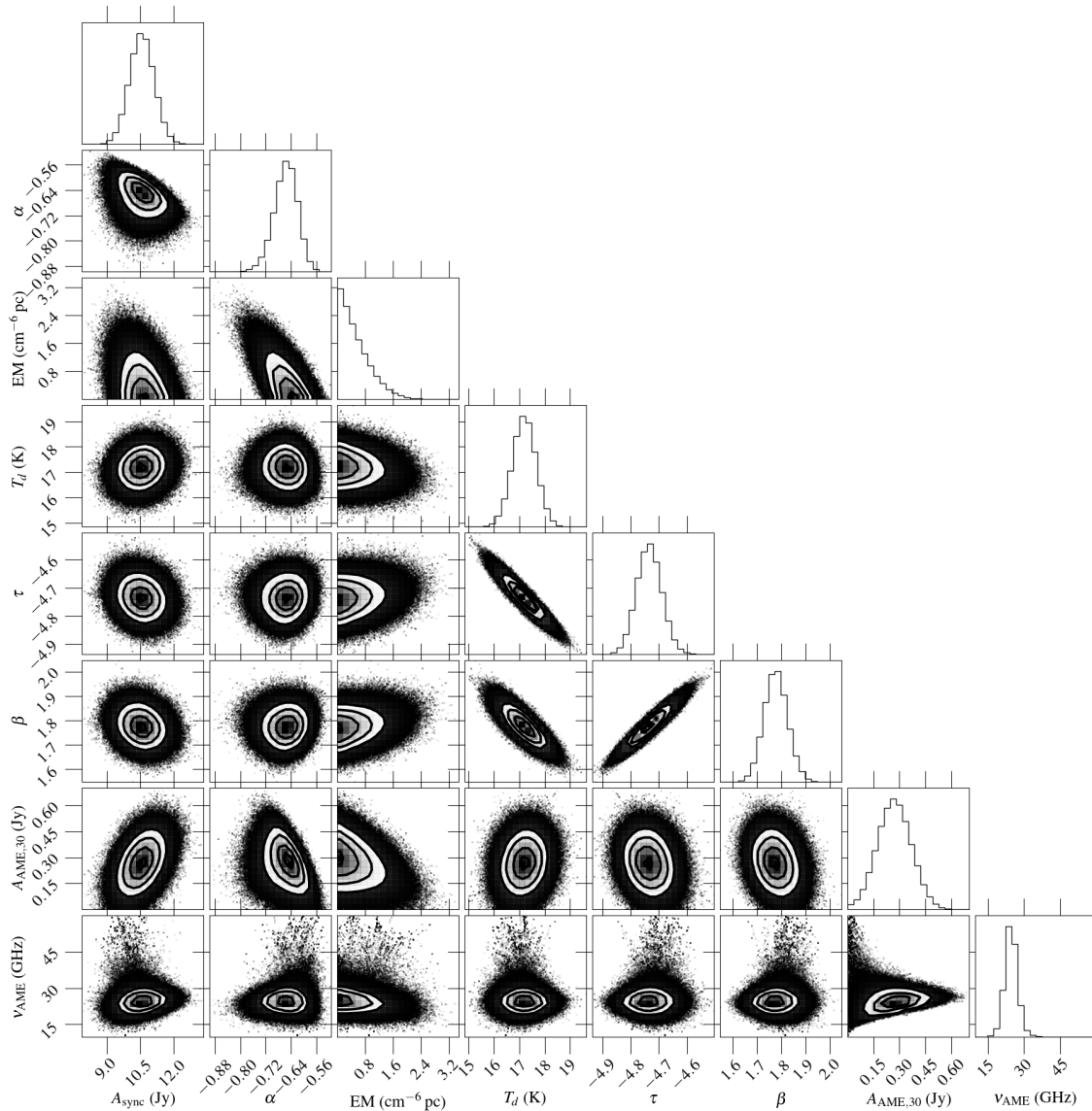


Figure 6. Posterior distributions for each parameter for the model shown in Figure 5. The model includes an AME component and a power-law synchrotron component, and has both CMB and background sources subtracted. The hard cut-off in the EM parameter is due to a positivity prior.

Criterion (AIC, Akaike 1974) of each model. As we are using nested models in the case of either including or excluding the spinning dust component (for columns under the "CMB & Source Subtracted" heading in Table 2) the AIC is an ideal tool for comparing the models. Instead of simply using the maximum likelihood value to determine the AIC we sum over the entire posterior to better account for biases due to non-Gaussian posterior distributions (Hilbe et al. 2017). We define the modified AIC as before in Equation 4.1. Although the AIC does not give a direct indication of the absolute quality of the fit, values can be compared between two nested models, with the lower AIC value indicating the model is a better representation of the data.

The AIC values in Table 2 show that fitting for AME after subtracting the CMB and point sources is slightly preferred (AIC = 106) over not including a spinning dust component (AIC = 119). Taking the difference of the AIC values for with and without spinning dust gives $\Delta\text{AIC} = 13$. In general, a $\Delta\text{AIC} > 4$ is considered significant (Hilbe et al. 2017), implying that we do detect spinning dust in the integrated spectrum of M 31.

We also tried fitting for spectral curvature in the spectral index of the synchrotron emission from M 31 using the same model given by Equation 13. We found that the curved synchrotron model had the same AIC and χ^2 values as the non-curved power-law spectrum. Fitting for a curved synchrotron component does not significantly change the AME component of M 31, but does double the observed emission measure. Given theoretical insights, particularly for our own Galaxy, that there is little evidence for synchrotron steepening or flattening with frequency (e.g. Strong et al. 2011) and that the curvature term was detected with low significance ($C = -0.04 \pm 0.03$), we prefer the model that includes no steepening. We give the best-fitting parameters including for the curved synchrotron component in Table 2 for reference.

6 DISCUSSION

6.1 Comparison of C-BASS with Other Radio Observations

The results presented in Section 5 are driven by the introduction of the C-BASS point at 4.76 GHz, where we measure a flux density of 4.04 ± 0.14 Jy. This is higher than the flux densities measured by the Effelsberg telescope (Berkhuijsen et al. 2003) at 4.85 GHz of 1.79 ± 0.20 Jy and the SRT (Battistelli et al. 2019) at 6.313 GHz of 1.207 ± 0.084 Jy, as shown in Figure 5.

The most likely reason for the difference in the flux densities between C-BASS and the other two surveys is the spatial filtering over a small area of the sky. The SRT and Effelsberg observations have resolutions of a few arcminutes, while C-BASS has 45 arcmin resolution. In general, it is difficult to measure the largest scales observed by a survey due to large-scale systematics from the receiver, atmosphere or surrounding environment. In this case, the largest scales measured by the SRT and Effelsberg are comparable to the size of M 31, as such these scales are more likely to be lost during data processing. Meanwhile, C-BASS observes the entire Northern hemisphere, and so preserving signal on scales of just a few degrees is considerably easier. We have verified this using end-to-end simulations to assess the impact of the C-BASS data processing and map-making on filtering the signal in the C-BASS map and found that there is no significant filtering beyond the first few multipoles and certainly none at scales of M 31 (the details of these simulations will be given in the upcoming C-BASS survey paper). Therefore, the difference in flux density is either because both the SRT and Effelsberg are filtering out emission from M 31, or possibly that C-BASS is adding in emission from our Galaxy that is filtered out in the higher resolution datasets. The latter is unlikely to be the case as we do not observe any bright Galactic background features in any of the lower resolution datasets and we effectively filter out scales larger than M 31 by subtracting a tight background annulus, as shown by the C-BASS data in Figure 2. However, evidence for filtering can be seen in the SRT data around bright point sources such as 5C 3.50 where a large negative ring surrounds the source.

To make a fair comparison with the lower resolution surveys requires replicating the filtering applied to the higher resolution data, which was attempted by Battistelli et al. (2019). This process can only be approximated, as the higher resolution information is not available in the low resolution surveys. By using C-BASS data, with a comparable resolution to these other surveys, we can make a fairer comparison of the total integrated flux density of M 31 without the need to make additional corrections.

6.2 Synchrotron Emission

We find that, for our favoured model including an AME component, a power-law synchrotron component, and with the CMB and background sources subtracted, the average synchrotron spectral index of M 31 is $\alpha = -0.66 \pm 0.03$. Synchrotron emission is the dominant emission component around 30 GHz—approximately twice the thermal free-free emission and AME contributions. The *Planck* analysis in Planck Collaboration et al. (2015) found a slightly steeper spectral index of $\alpha = -0.9 \pm 0.2$, however the inclusion of the C-BASS and QUIJOTE measurements show that the synchrotron spectrum is slightly flatter.

The 5 arcmin resolution analysis of M 31 using Effelsberg data at 2.645, 4.86, and 8.35 GHz (Beck et al. 2020) found a spectral index of $\alpha = -0.81 \pm 0.02$ for the non-thermal emission component—a value that lies between our analysis and that of the *Planck* analysis.

In Figure 5, we can see that the flux densities for M 31 observed by the Effelsberg data are approximately a factor of two lower than those predicted by the best-fit model using the C-BASS/QUIJOTE data. Comparing the synchrotron spectral indices from the Effelsberg and our analyses suggests that the estimate of the synchrotron spectral index from the 64-m SRT observations of $\alpha = -1.1 \pm 0.09$ (Battistelli et al. 2019; Fatigoni et al. 2021) is too steep—though all three are consistent with the *Planck* result of $\alpha = -0.92 \pm 0.16$ within 2σ . This is critical because a steeper synchrotron spectral index would imply a much lower synchrotron contribution at 30 GHz that in the SRT model is replaced by the large AME contribution predicted by the SRT model.

In the Milky Way, estimates of the spectral index of diffuse synchrotron emission are generally found in the range $-1.1 < \alpha < -1$ at WMAP and *Planck* frequencies (e.g., Davies et al. 2006; Dunkley et al. 2009; Harper et al. 2022), and flatten to $\beta \approx -2.7$ at frequencies of a few hundred MHz to 1 GHz (e.g. Lawson et al. 1987; Reich & Reich 1988). At higher frequencies it is possible that further steepening of the synchrotron spectrum can occur due to spectral aging of the cosmic ray electron (CRE) population (Strong et al. 2011), though observing spectral aging in diffuse synchrotron emission is challenging; the effect of spectral aging has been clearly seen in supernova remnants (e.g., Sun et al. 2011). To test for spectral curvature in M 31 we included a curvature term, shown in Equation 3. We found that when fitting the CMB and source subtracted M 31 spectrum with a three component fit of: free-free, thermal dust, and curved synchrotron emission the curvature term is $C = -0.007 \pm 0.017$, implying there is no significant detection of curvature. If we include AME in the fit, then the curvature term is $C = -0.04 \pm 0.03$ reducing the synchrotron contribution near 30 GHz; the excess flux density is then absorbed into the free-free component (but the AME amplitude remains unchanged). However, we find there is a $\approx 1\sigma$ constraint on the curvature, indicating that even an insignificant curvature in the M 31 synchrotron spectrum can have a significant impact on the estimation of other parameters—especially the free-free contribution.

6.3 Anomalous Microwave Emission in M31

We find a 3σ detection of AME in M 31 of 0.27 ± 0.09 Jy at 30 GHz for the model where CMB and background sources are subtracted, and there is no synchrotron spectral curvature. Though the exact significance changes slightly between models, in all cases where the spinning dust model is included (and the CMB is subtracted) we detect AME at similar levels of significance. For the case where the CMB is not subtracted but instead fitted in the spectrum, we find that there is a barely significant detection (1.2σ) of AME at 0.18 ± 0.15 Jy at 30 GHz. This reduction in significance when not subtracting the CMB is because the frequency range where AME peaks is the same as the frequencies where the CMB is the dominant component, 30–100 GHz.

We find an AME amplitude that is less than the amplitude predicted from the Planck Collaboration et al. (2015) analysis of $S_{\text{AME},30} = 0.7 \pm 0.3$ Jy at 30 GHz, and is much less than the predicted integrated AME flux density from the SRT analysis of $S_{\text{AME},25} = 1.4 \pm 0.2$ Jy at 25 GHz. The inclusion of the 4.76 GHz C-BASS data is the key difference between these analyses as it allows for the synchrotron emission at high frequencies to be constrained as discussed in Section 6.2.

We find that the AME brightness at 30 GHz relative to the dust opacity at 353 GHz, often referred to as AME emissivity, has a value of 0.17 ± 0.07 K/ τ_{353} —assuming a uniform brightness over our entire nominal aperture. This is much smaller than the AME emissivity

found in Galactic sources with well-measured AME, which typically has a value in the range $5\text{--}10\text{ K}/\tau_{353}$ (Hensley et al. 2016; Harper et al. 2022) for cirrus regions, but can be as high as $23.9\text{ K}/\tau_{353}$ in particular molecular clouds (Planck Collaboration et al. 2011).

We would expect that the average AME emissivity in M31 to be lower than what is found in targeted observations of AME sources. This is because we do not expect that AME to be uniformly distributed throughout the ISM in M31 or any galaxy. Moreover, the integrated spectrum of M31 is dominated by bright synchrotron and free-free features, such as supernova remnants or HII regions, associated with the molecular disk. The integrated emission from HII regions is rarely found to be dominated by AME (e.g., Scaife et al. 2008; Paladini et al. 2015; Rennie et al. 2022). Instead, we are more likely to find AME associated with dust clouds at the edge of these HII regions, such as in the case of the HII region associated with λ -Orionis (e.g., Cepeda-Arroita et al. 2021). Similarly, bright supernova remnants in the Galactic plane tend to show little evidence of AME (e.g., Sun et al. 2011; Cruciani et al. 2016; Rennie et al. 2022). Therefore, if we assume M31 is similar to our own Galaxy, then the total integrated emission will be dominated by these regions that have little or no AME component, and therefore reduce the average AME emissivity.

The apparent lack of AME in the integrated emission of other galaxies in the $10\text{--}50\text{ GHz}$ range (Peel et al. 2011; Bianchi et al. 2022) is also likely due to the same dilution over the entire volume of the galaxy. However, more observations are needed to determine whether this is true in general. This point is further supported by observations of several galaxies (Murphy et al. 2012), including NGC 6946 (Hensley et al. 2015) and NGC 4725 (Murphy et al. 2018), which found AME within only a few extranuclear regions.

One reason why it is important to determine the contribution of AME to the integrated spectrum of galaxies in general is that free-free emission can be used to determine star-formation rates. It has been suggested that 30 GHz is an ideal target frequency where the synchrotron and thermal dust contributions are minimal (Murphy et al. 2011). If AME is also a significant contribution, then this will bias any SFR estimates to lower values.

6.4 Star-Formation in M31

Free-free emission is directly proportional to the star-formation rate of a galaxy (Murphy et al. 2011). Using the updated values for fitted emission measure, and an assumed electron temperature of 8000 K , we can estimate the star-formation rate of M31 using one of several derived scaling relations (Kennicutt 1998; Condon et al. 1998; Murphy et al. 2011). Here we adopt the relations given in Murphy et al. (2011). When fitting for spinning dust emission with a power-law synchrotron model we do not find a significant detection of the emission measure: $EM = 0.4 \pm 0.4\text{ cm}^{-6}\text{ pc}$, thus we can only put a 1σ upper limit on the expected star-formation rate of $< 0.12\text{ }M_{\odot}\text{ yr}^{-1}$. If we do not fit for AME, the EM is higher at $EM = 0.9 \pm 0.6\text{ cm}^{-6}\text{ pc}$, which corresponds to a flux density of $S_{\text{ff}} = 0.25 \pm 0.18\text{ Jy}$ at 30 GHz , and a star-formation rate of $0.12 \pm 0.09\text{ }M_{\odot}\text{ yr}^{-1}$. If we use the model including AME and a curved synchrotron component we find an emission measure similar to that found when not including the AME in the synchrotron power-law model: $EM = 1.1 \pm 0.8\text{ cm}^{-6}\text{ pc}$, or $S_{\text{ff}} = 0.33 \pm 0.23\text{ Jy}$ at 30 GHz , corresponding to a star-formation rate of $0.16 \pm 0.12\text{ }M_{\odot}\text{ yr}^{-1}$.

The *Planck* analysis found a star-formation rate for M31 of $0.12\text{ }M_{\odot}\text{ yr}^{-1}$, which is consistent within 1σ with our estimates. Estimates of the star-formation rate from H α give $0.44\text{ }M_{\odot}\text{ yr}^{-1}$ (Azimlu et al. 2011), IR/UV comparisons estimate $0.25 \pm 0.05\text{ }M_{\odot}\text{ yr}^{-1}$ (Ford et al. 2013), and Xu & Helou (1996) estimated $0.36 \pm 0.14\text{ }M_{\odot}\text{ yr}^{-1}$

using IRAS data. All of which are several times higher than the star-formation rates we have predicted from the integrated free-free emission of M31.

The finding that all the estimates of the total star-formation rate of M31 using continuum free-free emission are lower than those found using other tracers is surprising. There have been multiple surveys of the integrated emission from other galaxies that show that, in general, free-free estimates of star-formation rates are consistent with other tracers (e.g., Murphy et al. 2011), however, AME is never included in these models, and generally there is only one measurement around the AME peak. There are several possible explanations for why our estimates of the star-formation rates are lower than expected. First, clearly the choice of model for the SED is critical, where models including AME predicted a systematically lower free-free emission contribution. However, the AME amplitude is robust and is supported by the data. Possibly then this indicates that the synchrotron emission spectrum is steepening at high frequencies, but even then our star-formation rates are lower than those predicted by other tracers.

Another possible reason for the differences in star-formation rates relates to the models used to calibrate the star-formation rates derived for the different tracers. The calibration of star-formation tracers depends on assumptions about the initial mass function and stellar evolution models (Kennicutt 1998), which when measuring the star-formation rate from the global integrated emission, as we have done, can be very different to those of individual local regions (Calzetti 2013), as was done for H α survey of M31 (Azimlu et al. 2011). Furthermore, when probing individual regions versus the global signal, very different timescales are being measured with the global signal being dominated by star-formation over the period of $10\text{--}100\text{ Myr}$, while local regions will be sensitive to more recent star-formation events of the order $1\text{--}10\text{ Myr}$ (Calzetti 2013).

A further factor to consider when comparing the star-formation rates derived from H α and UV to radio derived star-formation rates is the effect of dust. H α and UV tracers will suffer from attenuation due to dust along the line-of-sight. It is possible to correct for dust absorption but it becomes increasingly difficult, and with larger uncertainties, as the dust opacity becomes large. If the attenuation due to dust is over corrected, then this would bias the H α and UV estimates high.

Ultimately, it is difficult, given the large uncertainties on all of the star-formation rates presented, to give a definitive answer to the global star-formation rate of M31 other than it is approximately $0.3\text{ }M_{\odot}\text{ yr}^{-1}$. Additionally, we cannot rule out that AME dominates free-free emission in the global integrated signal of M31. This is critical to determine as free-free emission at 30 GHz is commonly used to determine star-formation rates in surveys such as COLDz (Algera et al. 2022), and if AME generally dominates over free-free at 30 GHz for other galaxies then this would bias star-formation rate estimates high. To answer this question will require future observations of M31 at arcminute resolutions so that the AME and free-free emission components of individual star-forming regions can be measured.

7 CONCLUSIONS

We have presented a new measurement of the integrated spectrum of M31, using C-BASS data as an additional constraint on the low-frequency emission. We find that the integrated spectrum of M31 at microwave frequencies has contributions from synchrotron, free-free, and AME. Similarly to Planck Collaboration et al. (2015), we find that AME is marginally detected with a 3σ significance of

0.27 ± 0.09 Jy. Further, we find that the average AME emissivity integrated over all of M 31 to be 0.17 ± 0.07 K/ τ_{353} . This is much lower than the typical value found for AME sources; since we are measuring the average AME emissivity, this implies that the AME must not be uniformly distributed throughout M 31—this is similar to what is observed in our Galaxy and other galaxies where AME has been observed (e.g., Hensley et al. 2015). We have showed that there are significant differences between the low-frequency fluxes observed by low resolution surveys like C-BASS and QUIJOTE, and the high resolution observations by the SRT (Battistelli et al. 2019) and Effelsberg (Berkhuijsen et al. 2003) that we expect are due to filtering of large-scale emission in the data processing of the high resolution data.

We attempted to fit the spectrum of M 31 using both power-law and curved power-law models of synchrotron emission. Although there is no statistical preference for synchrotron spectral curvature, the curved synchrotron models resulted in a higher emission measure and star-formation rate estimates that are more consistent with other star-formation tracers, but were still a factor of two or more lower. Therefore, we cannot entirely rule out the possibility of the synchrotron spectrum steepening at higher frequencies.

In conclusion, we find tentative evidence for AME within M 31; however, the low average emissivity suggests that it is not uniformly distributed throughout the ISM and instead is localised to smaller sub-regions within the galaxy. Recent results using dedicated observations of M 31 from the QUIJOTE MFI are consistent with our results when using the same aperture photometry (Fernández-Torreiro et al. 2023). However, the main results of the QUIJOTE analysis used the smaller apertures that match those given in Battistelli et al. (2019), and in this case they find an AME flux density that is three times higher than what we find, and subsequently a much fainter (and steeper— $\alpha = -0.99 \pm 0.21$) synchrotron contribution. This clearly shows the importance of both constraining the low frequency synchrotron emission with data like C-BASS and also the choice of aperture that is used. Ultimately, there remains some uncertainty regarding the nature of AME within M 31 that will require future follow-up observations at frequencies around the peak of the AME spectrum (20–30 GHz) with arcminute resolution that can resolve individual AME emitting regions. Such observations are already underway at both 22 GHz with the SRT (Fatigoni et al. 2021), and at 30 GHz with COMAP (Cleary et al. 2022).

ACKNOWLEDGEMENTS

The C-BASS project (<http://cbass.web.ox.ac.uk>) is a collaboration between Oxford and Manchester Universities in the UK, the California Institute of Technology in the U.S.A., Rhodes University, UKZN and the South African Radio Observatory in South Africa, and the King Abdulaziz City for Science and Technology (KACST) in Saudi Arabia. It has been supported by the NSF awards AST-0607857, AST-1010024, AST-1212217, and AST-1616227, and NASA award NNX15AF06G, the University of Oxford, the Royal Society, STFC, and the other participating institutions. SEH, CD, and JPL acknowledge support from an STFC Consolidated Grant (ST/P000649/1). This research was also supported by the South African Radio Astronomy Observatory, which is a facility of the National Research Foundation, an agency of the Department of Science and Technology. We would like to thank Russ Keeney for technical help at OVRO. We make use of the HEALPIX package (Górski et al. 2005), IDL astronomy library and Python ASTROPY (Astropy Collaboration et al. 2013, 2018), MATPLOTLIB (Hunter 2007), NUMPY

(Harris et al. 2020), HEALPY (Zonca et al. 2019), CORNER (Foreman-Mackey 2016) and SCIPY (Virtanen et al. 2020) packages. This research has made use of the NASA/IPAC Extragalactic Database (NED) which is operated by the Jet Propulsion Laboratory, California Institute of Technology, under contract with the National Aeronautics and Space Administration. This research has also made use of data from the OVRO 40-m monitoring program (Richards et al. 2011), supported by private funding from the California Institute of Technology and the Max Planck Institute for Radio Astronomy, and by NASA grants NNX08AW31G, NNX11A043G, and NNX14AQ89G and NSF grants AST-0808050 and AST-1109911. Some of the presented results are based on observations obtained with the QUIJOTE experiment (<http://research.iac.es/proyecto/quiote>).

APPENDIX A: SOURCE CATALOGUES

The integrated flux density of extragalactic point sources near M 31 are comparable to the total integrated flux of M 31 itself at lower frequencies ($\lesssim 20$ GHz) (Berkhuijsen et al. 2003). Therefore modelling and separating these background sources is critical to correctly estimate the relative contributions of free-free, synchrotron, and spinning dust emission associated with M 31. Also, flat spectrum sources (e.g., AGN) can turn over at frequencies of tens of gigahertz (Rani et al. 2011) mimicking a spinning dust spectrum. Fainter source populations tend towards a uniform Gaussian distribution across the sky, and hence will provide a similar flux density in both the annulus and aperture used for aperture photometry, i.e., they form part of the quasi-uniform background when the number of sources is large. We are primarily concerned with the brightest sources that contribute within the vicinity of M 31, which can strongly bias the photometry.

We used the NRAO VLA Sky Survey (NVSS Condon et al. 1998) catalogue to select bright sources at 1.4 GHz within a region containing the aperture and background annulus centred on M 31. We cross-referenced each source using the NASA/IPAC Extragalactic Database (NED)⁷ to confirm each source was not associated with M 31 itself. We used the historical photometry data available from NED to construct models for each source (Section 4.1) and then used these models to create point source maps at each frequency band that were then subtracted from the original data. All sources with only one frequency were discarded, and we also discarded one source with a rising spectrum, as the model predicted it would be extremely bright at microwave and sub-mm frequencies but this was not seen in any of the continuum surveys. After discarding bad sources, we were left with 71 sources to construct our background source maps. Most of the background radio sources contribute less than a few percent of the total flux density from M 31 except for the variable AGN 5C 3.50 that has a flux density at 5 and 30 GHz comparable to M 31. A full summary of the modelled background radio sources is given in Table A1. In Figure 3 we show the fitted spectrum of 5C 3.50, which uses a combination of radio and infrared data to define the spectrum. For all other sources we fitted the models to just the available radio data. Figure A1 shows examples of the fits to the second and third most bright radio sources near M 31.

DATA AVAILABILITY

All model fits for M 31 and radio sources can be made available upon request. Ancillary datasets described in Section 2.2 are available via

⁷ <https://ned.ipac.caltech.edu>

Table A1. Modelled point sources within the photometry aperture around M 31 in order of brightness at 5 GHz. Sources are selected from the NVSS 1.4 GHz survey (Condon et al. 1998) and cross-checked in the NED extragalactic source database. All source names use the NVSS designation except 5C 3.50, which is referenced in the main text. Sources that did not include ancillary data at more than one frequency or had steeply rising spectra are excluded. The source flux densities are from the model fits (see Section 4.1 for details).

Source	R.A. (J2000)	Dec. (J2000)	Angular Sep. (arcmin)	408 MHz Flux Density (Jy)	5 GHz Flux Density (mJy)	30 GHz Flux Density (mJy)	Model
5C 3.50 (B3 0035+413)	00 ^h 38 ^m 24.84 ^s	+41°37′06.00″	52.91	604.8 ± 63.7	553.1 ± 56.5	518.9 ± 54.3	Broken Power Law
NVSS J004217+400948	00 ^h 42 ^m 17.46 ^s	+40°09′48.5″	66.50	1892.7 ± 98.2	200.4 ± 8.7	28.1 ± 4.7	Curved Power Law
NVSS J004647+390046	00 ^h 46 ^m 47.52 ^s	+39°00′46.6″	143.12	112.9 ± 18.1	191.6 ± 10.6	70.5 ± 10.1	Curved Power Law
NVSS J004812+402152	00 ^h 48 ^m 12.94 ^s	+40°21′52.6″	82.55	1516.1 ± 85.5	136.8 ± 8.6	24.5 ± 2.9	Power Law
NVSS J004439+424801	00 ^h 44 ^m 39.17 ^s	+42°48′01.4″	94.36	1325.0 ± 81.5	124.0 ± 4.7	22.8 ± 1.6	Power Law
NVSS J003235+394215	00 ^h 32 ^m 35.51 ^s	+39°42′15.5″	148.97	992.6 ± 49.8	118.7 ± 9.0	26.0 ± 3.6	Power Law
NVSS J004218+412926	00 ^h 42 ^m 18.71 ^s	+41°29′26.8″	14.15	1026.9 ± 67.7	113.2 ± 4.3	23.4 ± 1.7	Power Law
NVSS J004802+393726	00 ^h 48 ^m 02.06 ^s	+39°37′26.6″	115.75	220.3 ± 14.5	111.6 ± 8.2	68.7 ± 9.7	Power Law
NVSS J003506+423818	00 ^h 35 ^m 06.02 ^s	+42°38′18.4″	118.34	923.9 ± 64.3	110.0 ± 9.7	24.0 ± 3.9	Power Law
NVSS J005331+402721	00 ^h 53 ^m 31.76 ^s	+40°27′21.5″	131.81	666.0 ± 45.7	88.3 ± 7.1	20.8 ± 3.0	Power Law
NVSS J005413+384214	00 ^h 54 ^m 13.78 ^s	+38°42′14.5″	202.79	188.7 ± 45.2	82.4 ± 4.7	45.5 ± 10.2	Power Law
NVSS J005832+390209	00 ^h 58 ^m 32.28 ^s	+39°02′09.2″	225.30	310.7 ± 82.3	81.7 ± 13.6	31.4 ± 13.7	Power Law
NVSS J005455+382150	00 ^h 54 ^m 55.87 ^s	+38°21′50.9″	223.84	1261.7 ± 65.8	77.1 ± 4.9	10.5 ± 1.2	Power Law
NVSS J003035+421128	00 ^h 30 ^m 35.15 ^s	+42°11′28″	146.81	114.9 ± 75.6	69.4 ± 10.9	48.5 ± 18.6	Power Law
NVSS J003216+400711	00 ^h 32 ^m 16.24 ^s	+40°07′11.2″	137.51	285.1 ± 19.8	66.0 ± 4.9	23.2 ± 3.3	Power Law
NVSS J004154+392521	00 ^h 41 ^m 54.96 ^s	+39°25′21″	111.16	1026.5 ± 50.4	65.5 ± 2.4	9.2 ± 0.6	Power Law
NVSS J005332+403443	00 ^h 53 ^m 32.35 ^s	+40°34′43.6″	129.27	420.0 ± 37.1	63.5 ± 10.7	16.5 ± 4.9	Power Law
NVSS J004843+404458	00 ^h 48 ^m 43.83 ^s	+40°44′58.5″	74.68	358.7 ± 23.6	62.1 ± 5.0	17.7 ± 2.7	Power Law
NVSS J004654+435328	00 ^h 46 ^m 54.58 ^s	+43°53′28.3″	163.97	410.5 ± 31.7	58.7 ± 4.6	14.6 ± 2.2	Power Law
NVSS J003638+425229	00 ^h 36 ^m 38.62 ^s	+42°52′29.2″	117.83	1196.9 ± 70.6	57.9 ± 4.2	6.6 ± 0.9	Power Law
NVSS J004755+394900	00 ^h 47 ^m 55.49 ^s	+39°49′00.2″	105.31	180.0 ± 19.9	56.2 ± 9.2	24.4 ± 7.2	Power Law
NVSS J004441+382957	00 ^h 44 ^m 41.56 ^s	+38°29′57.9″	167.67	135.2 ± 17.2	55.8 ± 2.8	29.7 ± 3.7	Power Law
NVSS J003111+394156	00 ^h 31 ^m 11.43 ^s	+39°41′56.1″	161.89	439.3 ± 26.3	55.6 ± 6.3	12.7 ± 2.6	Power Law
NVSS J003018+380355	00 ^h 30 ^m 18.81 ^s	+38°03′55.4″	239.76	227.9 ± 18.6	53.2 ± 3.7	18.8 ± 2.6	Power Law
NVSS J003525+394047	00 ^h 35 ^m 25.6 ^s	+39°40′47.7″	126.63	330.8 ± 22.1	53.0 ± 4.0	14.3 ± 1.9	Power Law
NVSS J004354+404634	00 ^h 43 ^m 54.35 ^s	+40°46′34.2″	32.39	421.0 ± 30.9	52.5 ± 4.8	11.9 ± 2.1	Power Law
NVSS J003022+381723	00 ^h 30 ^m 22.53 ^s	+38°17′23.2″	228.52	634.9 ± 36.2	52.3 ± 5.9	8.8 ± 1.8	Power Law
NVSS J004601+435517	00 ^h 46 ^m 01.85 ^s	+43°55′17.4″	163.28	819.8 ± 63.1	51.9 ± 8.8	7.2 ± 2.2	Power Law
NVSS J003419+424659	00 ^h 34 ^m 19.26 ^s	+42°46′59.4″	130.55	593.3 ± 45.3	51.7 ± 4.6	9.0 ± 1.5	Power Law
NVSS J005405+412515	00 ^h 54 ^m 05.78 ^s	+41°25′15.2″	128.28	170.0 ± 17.6	51.2 ± 7.8	21.7 ± 5.7	Power Law
NVSS J005744+415410	00 ^h 57 ^m 44.68 ^s	+41°54′10.8″	172.65	404.2 ± 25.3	51.1 ± 5.8	11.6 ± 2.3	Power Law
NVSS J004349+383010	00 ^h 43 ^m 49.42 ^s	+38°30′10.1″	166.42	684.4 ± 38.3	49.3 ± 6.1	7.5 ± 1.7	Power Law
NVSS J003137+391904	00 ^h 31 ^m 37.9 ^s	+39°19′04.3″	172.70	472.0 ± 34.7	49.0 ± 6.5	9.7 ± 2.4	Power Law
NVSS J003406+430242	00 ^h 34 ^m 06.03 ^s	+43°02′42.8″	143.44	410.1 ± 29.0	48.8 ± 5.4	10.7 ± 2.1	Power Law
NVSS J004358+393756	00 ^h 43 ^m 58.38 ^s	+39°37′56.6″	99.19	378.4 ± 23.0	48.6 ± 3.6	11.2 ± 1.5	Power Law
NVSS J005044+381310	00 ^h 50 ^m 44.93 ^s	+38°13′10.8″	204.95	423.6 ± 30.2	48.4 ± 2.9	10.3 ± 1.3	Power Law
NVSS J003428+403556	00 ^h 34 ^m 28.73 ^s	+40°35′56.4″	101.80	385.7 ± 26.8	48.4 ± 6.2	11.0 ± 2.6	Power Law
NVSS J003007+433524	00 ^h 30 ^m 07.93 ^s	+43°35′24.2″	197.11	220.3 ± 16.2	45.0 ± 5.1	14.5 ± 2.9	Power Law
NVSS J003641+380903	00 ^h 36 ^m 41.28 ^s	+38°09′03.8″	199.63	675.3 ± 33.3	44.0 ± 6.1	6.2 ± 1.5	Power Law
NVSS J003039+423704	00 ^h 30 ^m 39.67 ^s	+42°37′04.9″	157.14	309.9 ± 24.8	43.8 ± 7.3	10.8 ± 3.1	Power Law
NVSS J004824+431931	00 ^h 48 ^m 24.46 ^s	+43°19′31.2″	138.53	209.2 ± 17.8	43.3 ± 3.0	14.0 ± 2.0	Power Law
NVSS J003048+411053	00 ^h 30 ^m 48.78 ^s	+41°10′53.7″	134.58	1232.7 ± 73.3	43.3 ± 2.7	3.9 ± 0.4	Power Law
NVSS J005213+424102	00 ^h 52 ^m 13.75 ^s	+42°41′02.9″	135.73	462.9 ± 30.3	42.9 ± 5.6	7.8 ± 1.8	Power Law
NVSS J003736+393812	00 ^h 37 ^m 36.72 ^s	+39°38′12.4″	114.03	192.8 ± 21.0	42.1 ± 1.8	0.3 ± 0.1	Curved Power Law
NVSS J004844+395331	00 ^h 48 ^m 44.72 ^s	+39°53′31.5″	107.29	304.5 ± 21.2	41.7 ± 3.1	10.0 ± 1.4	Power Law
NVSS J005537+383212	00 ^h 55 ^m 37.54 ^s	+38°32′12.2″	221.04	264.9 ± 18.9	41.6 ± 4.7	11.1 ± 2.2	Power Law
NVSS J003719+385916	00 ^h 37 ^m 19.29 ^s	+38°59′16.5″	150.25	590.0 ± 43.4	41.1 ± 6.0	6.1 ± 1.6	Power Law
NVSS J003848+411607	00 ^h 38 ^m 48.28 ^s	+41°16′07.4″	44.29	170.0 ± 19.4	39.0 ± 3.0	13.6 ± 2.0	Power Law
NVSS J005411+421634	00 ^h 54 ^m 11.47 ^s	+42°16′34.8″	141.71	463.1 ± 29.4	36.2 ± 3.3	5.9 ± 0.9	Power Law
NVSS J003956+411138	00 ^h 39 ^m 56.35 ^s	+41°11′38.4″	31.84	187.1 ± 14.2	36.2 ± 6.0	11.2 ± 3.2	Power Law
NVSS J005351+424936	00 ^h 53 ^m 51.6 ^s	+42°49′36.1″	155.23	120.0 ± 18.9	35.5 ± 5.9	14.8 ± 4.8	Power Law
NVSS J005540+393337	00 ^h 55 ^m 40.34 ^s	+39°33′37.8″	179.81	469.2 ± 35.2	35.3 ± 5.6	5.5 ± 1.6	Power Law
NVSS J004942+382259	00 ^h 49 ^m 42.41 ^s	+38°22′59.5″	190.84	226.2 ± 15.7	35.3 ± 6.2	9.3 ± 2.8	Power Law
NVSS J005755+424606	00 ^h 57 ^m 55.38 ^s	+42°46′06.1″	191.68	200.0 ± 19.9	35.2 ± 5.7	10.2 ± 2.9	Power Law
NVSS J005057+420452	00 ^h 50 ^m 57.43 ^s	+42°04′52.1″	104.24	242.8 ± 21.0	35.0 ± 5.5	8.7 ± 2.5	Power Law
NVSS J004653+394254	00 ^h 46 ^m 53.45 ^s	+39°42′54.4″	104.58	130.0 ± 21.6	34.4 ± 4.9	13.3 ± 3.7	Power Law
NVSS J005110+383842	00 ^h 51 ^m 10.93 ^s	+38°38′42.5″	184.96	140.0 ± 19.0	34.4 ± 4.5	12.6 ± 3.0	Power Law
NVSS J004648+420855	00 ^h 46 ^m 48.11 ^s	+42°08′55.5″	69.74	400.7 ± 23.5	33.9 ± 4.8	5.8 ± 1.4	Power Law

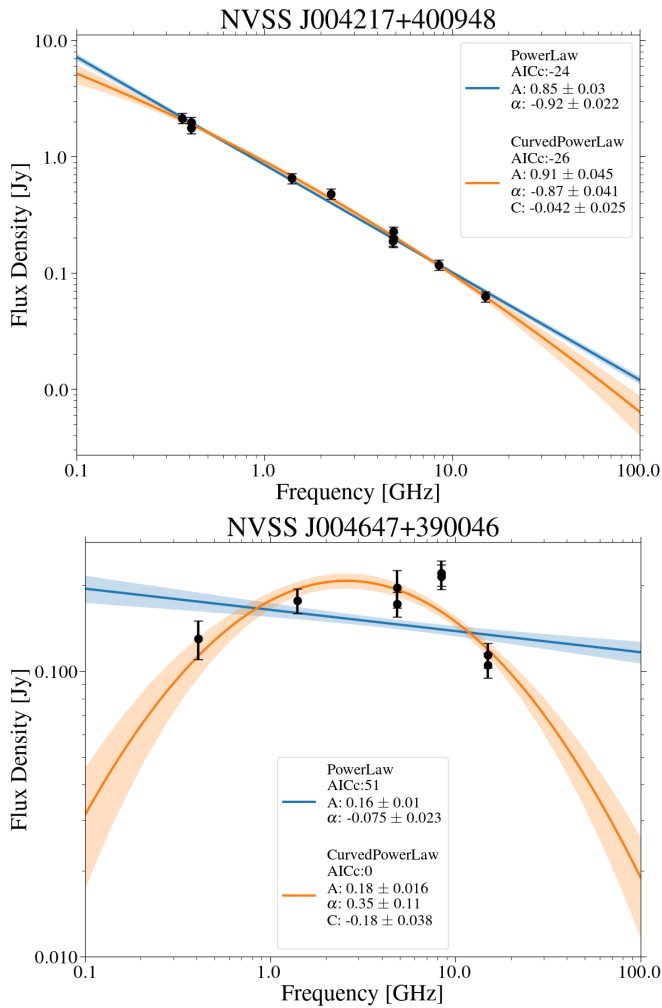


Figure A1. Best fit power-law and curved power-law models to the radio data for NVSS J004217+400948 (top) and NVSS J004647+390046 (bottom). The best fit parameters and AICc values for each model are shown in the legend.

from the papers cited, the NASA LAMBDA website, or the *Planck* legacy archive. The C-BASS map is not currently available but will be published (Taylor et al., in prep.) and released in the near future.

REFERENCES

Akaike H., 1974, *IEEE Transactions on Automatic Control*, 19, 716
 Algera H. S. B., et al., 2022, *ApJ*, 924, 76
 Ali-Haïmoud Y., Hirata C. M., Dickinson C., 2009, *MNRAS*, 395, 1055
 Astropy Collaboration et al., 2013, *A&A*, 558, A33
 Astropy Collaboration et al., 2018, *AJ*, 156, 123
 Azimlu M., Marciniak R., Barmby P., 2011, *AJ*, 142, 139
 Battistelli E. S., et al., 2019, *ApJ*, 877, L31
 Beck R., Berkhuijsen E. M., Wielebinski R., 1980, *Nature*, 283, 272
 Beck R., Berkhuijsen E. M., Gießbübel R., Mulcahy D. D., 2020, *A&A*, 633, A5
 Bennett C. L., et al., 2013, *ApJS*, 208, 20
 Berkhuijsen E. M., Wielebinski R., Beck R., 1983, *A&A*, 117, 141
 Berkhuijsen E. M., Beck R., Hoernes P., 2003, *A&A*, 398, 937
 Bianchi S., et al., 2022, *A&A*, 658, L8
 Brown R. H., Hazard C., 1950, *Nature*, 166, 901

Byrd R. H., Lu P., Nocedal J., Zhu C., 1995, *SIAM Journal on Scientific Computing*, 16, 1190
 Calzetti D., 2013, in Falcón-Barroso J., Knapen J. H., eds., *Secular Evolution of Galaxies*. Cambridge University Press, p. 419, doi:10.48550/arXiv.1208.2997
 Cardoso J.-F., Le Jeune M., Delabrouille J., Betoule M., Patanchon G., 2008, *IEEE Journal of Selected Topics in Signal Processing*, 2, 735
 Casassus S., et al., 2008, *MNRAS*, 391, 1075
 Cepeda-Arroita R., et al., 2021, *MNRAS*, 503, 2927
 Cleary K. A., et al., 2022, *ApJ*, 933, 182
 Code A. D., Welch G. A., 1979, *ApJ*, 228, 95
 Condon J. J., Cotton W. D., Greisen E. W., Yin Q. F., Perley R. A., Taylor G. B., Broderick J. J., 1998, *AJ*, 115, 1693
 Cruciani A., et al., 2016, *MNRAS*, 459, 4224
 Davies R. D., Dickinson C., Banday A. J., Jaffe T. R., Górski K. M., Davis R. J., 2006, *MNRAS*, 370, 1125
 De Paolis F., et al., 2014, *A&A*, 565, L3
 Delabrouille J., Cardoso J. F., Le Jeune M., Betoule M., Fay G., Guilloux F., 2009, *A&A*, 493, 835
 Dickinson C., et al., 2018, *New Astron. Rev.*, 80, 1
 Draine B. T., 2011, *Physics of the Interstellar and Intergalactic Medium*. Princeton University Press
 Draine B. T., Lazarian A., 1998, *ApJ*, 508, 157
 Dunkley J., et al., 2009, *ApJ*, 701, 1804
 Eriksen H. K., Jewell J. B., Dickinson C., Banday A. J., Górski K. M., Lawrence C. R., 2008, *ApJ*, 676, 10
 Fatigoni S., et al., 2021, *A&A*, 651, A98
 Fernández-Cobos R., Vielva P., Barreiro R. B., Martínez-González E., 2012, *MNRAS*, 420, 2162
 Fernández-Torreiro M., et al., 2023, *arXiv e-prints*, p. arXiv:2305.08547
 Ford G. P., et al., 2013, *ApJ*, 769, 55
 Foreman-Mackey D., 2016, *The Journal of Open Source Software*, 1, 24
 Foreman-Mackey D., et al., 2019, *The Journal of Open Source Software*, 4, 1864
 Fritz J., et al., 2012, *A&A*, 546, A34
 Fuskeland U., Wehus I. K., Eriksen H. K., Naess S. K., 2014, *ApJ*, 790, 104
 Gelman A., Rubin D. B., 1992, *Statistical Science*, 7, 457
 Gordon K. D., et al., 2006, *ApJ*, 638, L87
 Górski K. M., Hivon E., Banday A. J., Wandelt B. D., Hansen F. K., Reinecke M., Bartelmann M., 2005, *ApJ*, 622, 759
 Harper S. E., et al., 2022, *MNRAS*, 513, 5900
 Harris C. R., et al., 2020, *Nature*, 585, 357
 Haslam C. G. T., Klein U., Salter C. J., Stoffel H., Wilson W. E., Cleary M. N., Cooke D. J., Thomasson P., 1981, *A&A*, 100, 209
 Haslam C. G. T., Salter C. J., Stoffel H., Wilson W. E., 1982, *A&AS*, 47, 1
 Hauser M. G., et al., 1998, *ApJ*, 508, 25
 Hensley B., Murphy E., Staguhn J., 2015, *MNRAS*, 449, 809
 Hensley B. S., Draine B. T., Meisner A. M., 2016, *ApJ*, 827, 45
 Hilbe J. M., de Souza R. S., Ishida E. E. O., 2017, *Bayesian Models for Astrophysical Data Using R, JAGS, Python, and Stan*. Cambridge University Press, doi:10.1017/CBO9781316459515
 Holler C. M., et al., 2013, *IEEE Transactions on Antennas and Propagation*, 61, 117
 Hunter J. D., 2007, *Computing in Science & Engineering*, 9, 90
 Jones M. E., et al., 2018, *MNRAS*, 480, 3224
 Kennicutt Robert C. J., 1998, *ARA&A*, 36, 189
 King O. G., et al., 2014, *MNRAS*, 438, 2426
 Kogut A., Banday A. J., Bennett C. L., Górski K. M., Hinshaw G., Smoot G. F., Wright E. I., 1996, *ApJ*, 464, L5
 Kogut A., et al., 2007, *ApJ*, 665, 355
 Lauer T. R., et al., 1993, *AJ*, 106, 1436
 Lawson K. D., Mayer C. J., Osborne J. L., Parkinson M. L., 1987, *MNRAS*, 225, 307
 Leitch E. M., Readhead A. C. S., Pearson T. J., Myers S. T., 1997, *ApJ*, 486, L23
 Murphy E. J., et al., 2011, *ApJ*, 737, 67
 Murphy E. J., et al., 2012, *ApJ*, 761, 97

- Murphy E. J., Linden S. T., Dong D., Hensley B. S., Momjian E., Helou G., Evans A. S., 2018, *ApJ*, 862, 20
- Paladini R., Burigana C., Davies R. D., Maino D., Bersanelli M., Cappellini B., Platania P., Smoot G., 2003, *A&A*, 397, 213
- Paladini R., Ingallinera A., Agliozzo C., Tibbs C. T., Noriega-Crespo A., Umata G., Dickinson C., Trigilio C., 2015, *ApJ*, 813, 24
- Pauliny-Toth I. K., Shakeshaft J. R., 1962, *MNRAS*, 124, 61
- Peel M. W., Dickinson C., Davies R. D., Clements D. L., Beswick R. J., 2011, *MNRAS*, 416, L99
- Peel M. W., Genova-Santos R., Dickinson C., Leahy J. P., López-Caraballo C., Fernández-Torreiro M., Rubiño-Martín J. A., Spencer L. D., 2022, *Research Notes of the American Astronomical Society*, 6, 252
- Planck Collaboration et al., 2011, *A&A*, 536, A20
- Planck Collaboration et al., 2014, *A&A*, 565, A103
- Planck Collaboration et al., 2015, *A&A*, 582, A28
- Planck Collaboration et al., 2020a, *A&A*, 641, A1
- Planck Collaboration et al., 2020b, *A&A*, 643, A42
- Planck Collaboration XII 2014, *A&A*, 571, A12
- Rani B., et al., 2011, *MNRAS*, 417, 1881
- Reich P., Reich W., 1986, *A&AS*, 63, 205
- Reich P., Reich W., 1988, *A&A*, 196, 211
- Remazeilles M., Dickinson C., Banday A. J., Bigot-Sazy M.-A., Ghosh T., 2015, *MNRAS*, 451, 4311
- Rennie T. J., et al., 2022, *ApJ*, 933, 187
- Richards J. L., et al., 2011, *ApJS*, 194, 29
- Rubiño-Martín J. A., et al., 2023, *MNRAS*, 519, 3383
- Scaife A. M. M., et al., 2008, *MNRAS*, 385, 809
- Shetty R., Kauffmann J., Schnee S., Goodman A. A., Ercolano B., 2009, *ApJ*, 696, 2234
- Stevenson M. A., 2014, *ApJ*, 781, 113
- Strong A. W., Orlando E., Jaffe T. R., 2011, *A&A*, 534, A54
- Sun X. H., Reich P., Reich W., Xiao L., Gao X. Y., Han J. L., 2011, *A&A*, 536, A83
- Sutton D., et al., 2010, *MNRAS*, 407, 1387
- Tahir N., De Paolis F., Qadir A., Nucita A. A., 2022, *A&A*, 664, A30
- Virtanen P., et al., 2020, *Nature Methods*, 17, 261
- Watson R. A., Rebolo R., Rubiño-Martín J. A., Hildebrandt S., Gutiérrez C. M., Fernández-Cerezo S., Hoyland R. J., Battistelli E. S., 2005, *ApJ*, 624, L89
- Weiland J. L., et al., 2011, *ApJS*, 192, 19
- White R. L., Becker R. H., 1992, *ApJS*, 79, 331
- Xu C., Helou G., 1996, *ApJ*, 456, 152
- Ysard N., et al., 2012, *A&A*, 542, A21
- Zonca A., Singer L., Lenz D., Reinecke M., Rosset C., Hivon E., Gorski K., 2019, *Journal of Open Source Software*, 4, 1298

This paper has been typeset from a $\text{\TeX}/\text{\LaTeX}$ file prepared by the author.